



**HAL**  
open science

## Dust and Clouds on Mars: The View from Mars Express

Anni Määttänen, A. Fedorova, M. Giuranna, J. Hernández-Bernal, Yann Leseigneur, Franck Montmessin, Kevin S. Olsen, A. Sánchez-Lavega, A. Stcherbinine, A. Szantai, et al.

### ► To cite this version:

Anni Määttänen, A. Fedorova, M. Giuranna, J. Hernández-Bernal, Yann Leseigneur, et al.. Dust and Clouds on Mars: The View from Mars Express. *Space Science Reviews*, 2024, 220, pp.63. 10.1007/s11214-024-01092-z . hal-04677700

**HAL Id: hal-04677700**

**<https://hal.science/hal-04677700v1>**

Submitted on 26 Aug 2024

**HAL** is a multi-disciplinary open access archive for the deposit and dissemination of scientific research documents, whether they are published or not. The documents may come from teaching and research institutions in France or abroad, or from public or private research centers.

L'archive ouverte pluridisciplinaire **HAL**, est destinée au dépôt et à la diffusion de documents scientifiques de niveau recherche, publiés ou non, émanant des établissements d'enseignement et de recherche français ou étrangers, des laboratoires publics ou privés.



Distributed under a Creative Commons Attribution 4.0 International License



# Dust and Clouds on Mars: The View from Mars Express

A. Määttä<sup>1</sup> · A. Fedorova<sup>2</sup> · M. Giuranna<sup>3</sup> · J. Hernández-Bernal<sup>4</sup> · Y. Leseigneur<sup>5</sup> · F. Montmessin<sup>1</sup> · K.S. Olsen<sup>6</sup> · A. Sánchez-Lavega<sup>4</sup> · A. Stcherbinine<sup>7</sup> · A. Szantai<sup>8</sup> · D. Tirsch<sup>9</sup> · M. Vincendon<sup>5</sup> · Y. Willame<sup>10</sup> · P. Wolkenberg<sup>3</sup>

Received: 21 September 2023 / Accepted: 11 July 2024  
© The Author(s) 2024

## Abstract

European Space Agency's Mars Express (MEX) has been orbiting Mars for 20 years and its instruments have provided a plethora of observations of atmospheric dust and clouds. These observations have been analysed to produce many unique views of the processes leading to dust lifting and cloud formation, and a full picture of the climatologies of dust and clouds has emerged. Moreover, the orbit of MEX enables viewing the planet at many local times, giving a unique access to the diurnal variations of the atmosphere. This article provides an overview of the observations of dust and clouds on Mars by MEX, complemented by the Trace Gas Orbiter that has been accompanying MEX on orbit for some years.

**Keywords** Mars · Atmosphere · Clouds · Mineral dust

---

✉ A. Määttä  
[anni.maattanen@latmos.ipsl.fr](mailto:anni.maattanen@latmos.ipsl.fr)

✉ P. Wolkenberg  
[paulina.wolkenberg@inaf.it](mailto:paulina.wolkenberg@inaf.it)

<sup>1</sup> LATMOS/IPSL, Sorbonne Université, UVSQ Université Paris-Saclay, CNRS, Paris, France

<sup>2</sup> Space Research Institute of the Russian Academy of Sciences (IKI), Moscow, Russia

<sup>3</sup> Istituto Nazionale di Astrofisica, Istituto di Astrofisica e Planetologia Spaziali, Rome, Italy

<sup>4</sup> Universidad del País Vasco UPV/EHU, Escuela de Ingeniería de Bilbao, Departamento Física Aplicada, Bilbao, Spain

<sup>5</sup> Institut d'Astrophysique Spatiale, Université Paris-Saclay, CNRS, Orsay, 91405, France

<sup>6</sup> Department of Physics, University of Oxford, Oxford, UK

<sup>7</sup> Department of Astronomy and Planetary Science, Northern Arizona University, Flagstaff, AZ, USA

<sup>8</sup> Laboratoire de Météorologie Dynamique (LMD/IPSL), Sorbonne Université, Centre National de la Recherche Scientifique, École Normale Supérieure, École Polytechnique, Paris, France

<sup>9</sup> German Aerospace Center (DLR), Institute of Planetary Research, Berlin, Germany

<sup>10</sup> Royal Belgian Institute for Space Aeronomy, Brussels, Belgium

## 1 Introduction

Airborne dust is one of the major elements of the Martian atmosphere due to its radiative effect and consequent coupling with the dynamics on all spatial and temporal scales. Dust is constantly present in the atmosphere, although its concentration varies strongly throughout the Martian year and from region to region (Kahre et al., 2017). Atmospheric dust particles are deposited by sedimentation, whereas they are injected into the atmosphere by different processes: Winds in the form of localized gusts, vortices of convective nature (dust devils) and dust storms. Dust storms are the major disturbances injecting dust (see recent reviews: Kahre et al., 2017; Forget & Montabone, 2017) and are classified according to their horizontal extent and duration as local (area  $< 1.6 \times 10^6$  km<sup>2</sup>), regional (area  $> 1.6 \times 10^6$ – $10^7$  km<sup>2</sup>) and global (area  $> 10^7$  km<sup>2</sup>), the latter being also known as “Global Dust Storms” (GDSs), “Global Dust Events” (GDEs) or “Planet Encircling Dust Events” (PEDEs).

The main water ice cloud features observed on Mars are driven by the Martian seasons (Smith 2004). The cloud features affected by the summer-winter cycle are polar hoods that occur at high northern and southern latitudes during their respective winters. Mars arrives at perihelion while it is summer in the Southern Hemisphere (SH), resulting in an overall warmer atmosphere and higher airborne dust loading. Over this perihelion period, Mars is relatively free of long-lasting, low-altitude cloud formations at mid and low latitudes. Conversely, during spring and summer in the northern hemisphere (NH) (the aphelion season, or the first half of the Martian Year), the relatively cold atmosphere across both hemispheres above 10 km induces the condensation of water vapour and the formation of a large, very long-lasting band of low latitude cloud cover referred to as the aphelion cloud belt (ACB, Wang and Ingersoll 2002). Water ice clouds are also observed at smaller scales, often related to topographic features.

CO<sub>2</sub> ice clouds form also on Mars and the first spectroscopic identification of mesospheric CO<sub>2</sub> ice came from Mars Express (MEX; Montmessin et al. 2007). The mesospheric CO<sub>2</sub> ice clouds that form during the first half of the Martian year around the equator, but also at midlatitudes during local autumn, have since been detected with other instruments and missions.

Mars Express has studied all of these phenomena through a variety of observation modes and with a good spatial, seasonal and local time coverage. In this article we highlight the MEX achievements and discoveries in the field of aerosol and cloud research. A majority of MEX instruments, namely High Resolution Stereo Camera (HRSC, Gwinner et al. 2016), Observatoire pour la Minéralogie, l’Eau, les Glaces et l’Activité (OMEGA, Bibring et al. 2007), Planetary Fourier Spectrometer (PFS, Giuranna et al. 2021), Spectroscopy for the Investigation of the Characteristics of the Atmosphere of Mars (SPICAM, Montmessin et al. 2017), and Visual Monitoring Camera (VMC, Sánchez-Lavega et al. 2018a), have participated in this effort, supported in the last years by the Trace Gas Orbiter (TGO) instruments Atmospheric Chemistry Suite (ACS, Korabiev et al. 2018) and Nadir and Occultation for MArS Discovery (NOMAD, Vandaele et al. 2018). Detailed instrument descriptions can be found in the original instrument papers and in Wilson et al. (2024, this collection).

## 2 Dust

### 2.1 Global Climatology

Three instruments on MEX (PFS, SPICAM, and OMEGA) have monitored atmospheric dust. Here we describe the global dust climatology observed by these instruments. Figure 1

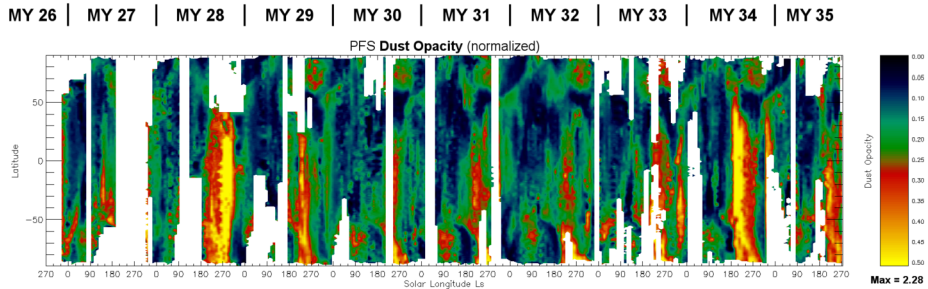


**Fig. 1** Zonal mean of column integrated dust optical depth (DOD) at  $1075\text{ cm}^{-1}$  ( $9.3\ \mu\text{m}$ ) as a function of latitude from  $L_s = 330^\circ$  of MY 26 to  $L_s = 270^\circ$  of MY 35 retrieved from PFS/MEX observations (Giuranna et al. 2021). The DOD is normalized to a reference pressure level of 6.1 mbar

reveals the overall behavior of Martian dust, showing the seasonal and latitudinal variation of zonal mean of total column dust optical depth (DOD) observed by PFS from MY 26 to MY 35 (see also Giuranna et al. 2021). The first half of the Martian Year is characterized by a nearly dust-free atmosphere with total DOD at an average level of  $\sim 0.15$ . Larger DOD of up to 0.4 are typically observed in the dusty second half of the year ( $L_s = 180^\circ\text{--}360^\circ$ ). The eight full MYs of PFS observations (Fig. 1) also contain two GDSs, one in MY 28 and one in MY 34, with zonal-mean DOD as high as 2. In MY 29 and 35 (i.e., the two MYs following the GDS events) a particularly strong regional dust storm was observed during the dusty season compared to the other MYs.

An averaged PFS climatology of dust (excluding the GDS years) is presented in Fig. 2 (Giuranna et al. 2021). Four main features with large DOD can be seen. However, the two features appearing in the polar winter regions are probably a result of dust being retrieved there instead of existing  $\text{CO}_2$  clouds due to overlapping spectral features in the  $7\text{--}25\ \mu\text{m}$  (McCleese et al. 2010, 2017; Heavens et al. 2011a, 2011b, 2011c). The third feature is seen as DOD as high as 0.5 extending from the South Pole up to  $30^\circ\text{N}$  from  $L_s = 210^\circ$  until  $L_s = 260^\circ$ . Dust activity there is very similar to the “type A” dust storm and with the “type B” dust storm seen later in the season near the South Pole (Kass et al. 2016). The fourth feature appearing during  $L_s = 310^\circ\text{--}330^\circ$  between  $60^\circ\text{S}$  and  $20^\circ\text{N}$  corresponds to the very short “type C” dust events (Kass et al. 2016).

Dynamic dust activity is regularly observed near the edges of the seasonal caps (black line in Fig. 2) in both hemispheres where several mechanisms can contribute to dust lifting (Siili et al. 1999; Toigo et al. 2002; Spiga and Lewis 2010; Mulholland et al. 2015). Increased dust storm activity at the cap edges was also observed by VMC, HRSC, Mars Orbiting Camera (MOC) and Hubble Space Telescope (HST) cameras (Cantor et al. 2001, 2002; Wang et al. 2003; James et al. 1999, 2005, Sánchez-Lavega et al. 2022), as well as by OMEGA (Douté 2014, Vincendon et al. 2008; Leseigneur and Vincendon 2023) and Thermal Emission Spectrometer (TES, Horne and Smith 2009). On the contrary, Mars Climate Sounder (MCS) limb observations show a clear atmosphere above the polar cap edges during winter solstice seasons (McCleese et al. 2010; Heavens et al. 2011b, 2011c; Montabone et al. 2015), suggesting that the dust activity is limited to the lowermost atmospheric layers. Indeed, MCS observes the atmosphere in limb geometry which has the disadvantage of not being able to observe the first kilometers above the ground. Retrievals below altitudes  $\sim 10\text{--}15\ \text{km}$  are often not possible due to opaqueness of the atmosphere, and the dust in the unretrieved part of the profile can account for a significant fraction of the total (column)

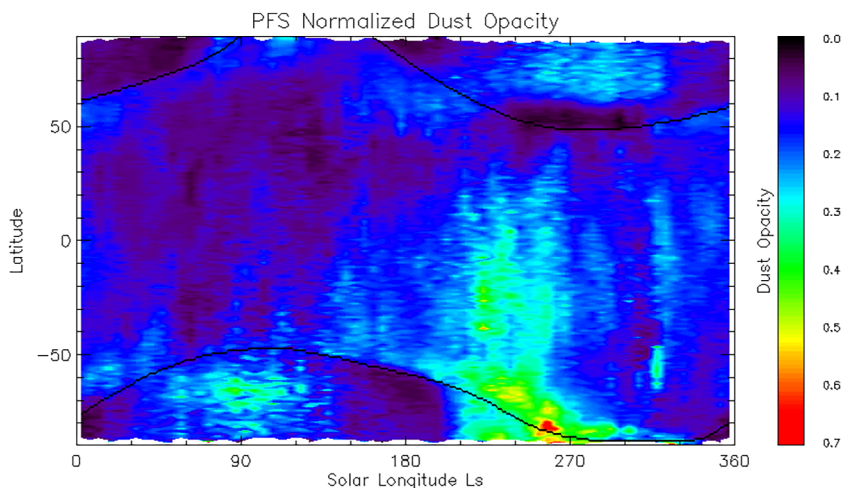


**Fig. 2** Seasonal and latitudinal variation of zonal-mean DOD at  $9.3\ \mu\text{m}$  observed by PFS. Data collected from all observed Martian years without GDSs are binned in  $5^\circ\ \text{Ls} \times 1^\circ$  latitude bins and normalized to a reference pressure level of 6.1 mbar. The black line shows the climatological latitude of the seasonal  $\text{CO}_2$  polar cap edges. Reproduced with permission from Giuranna et al. (2021), copyright by Elsevier

opacity (Montabone et al. 2015). A remarkably dust-free atmosphere is consistently observed at  $45^\circ\text{N}$  to  $60^\circ\text{N}$  during  $\text{L}_s = 220^\circ\text{--}310^\circ$  (see also Fig. 9 in Wolkenberg et al. 2018). This feature is also observed by TES and MCS and partially overlaps, both spatially and seasonally, with another puzzling feature observed by PFS: a region where practically no ice clouds form during the entire northern fall (see Sect. 3.1 and Fig. 8). This region is located where the descending branch of the Hadley circulation occurs and warms the atmosphere due to the adiabatic compression, but so far the formation of these features has not been explained.

The UV channel of the SPICAM instrument was used in Willame et al. (2017) to study the DOD column during more than four Martian years (MY26–30). The derived DOD climatology reproduced the expected year-to-year repeatability of the aphelion season characterized by a lower dust loading, except for some local dust storm events. The inter-annual variability of the perihelion season was also observed with several regional storms or the global dust storm event of MY28 that arose at different periods and locations. The results were in a good qualitative agreement with previous works obtained from TES and Thermal Emission Imaging System (THEMIS, Smith 2004, 2009), with the Montabone et al. (2015) climatology, and PFS observations (Giuranna et al. 2021).

The OMEGA dataset has also been used for different studies on atmospheric dust and a global monitoring of atmospheric dust was carried out by Leseigneur and Vincendon (2023). They developed a method to compute DOD at  $0.9\ \mu\text{m}$  and applied it to most OMEGA observations from the end of MY 26 to the beginning of MY 30. Figure 3 illustrates these results with a global map of maximum DOD values observed during this period (excluding the MY28 GDS). Maximum DODs are concentrated on dust storm travel routes such as the most significant Acidalia-Chryse channel ( $\sim 325^\circ\text{E}$ ), on dust source areas like Hellas Planitia ( $40\text{--}100^\circ\text{E}$ ,  $20\text{--}60^\circ\text{S}$ ), at polar latitudes (notably southern ones), on mid-latitude plains (e.g., Solis, Amazonis, Utopia, Isidis, Utopia, Elysium). Northern high latitude plains have much lower DODs. From these DOD measurements at  $0.9\ \mu\text{m}$ , particle sizes can also be deduced by comparing values in thermal-IR (e.g., MCS/MRO). For example, the dust

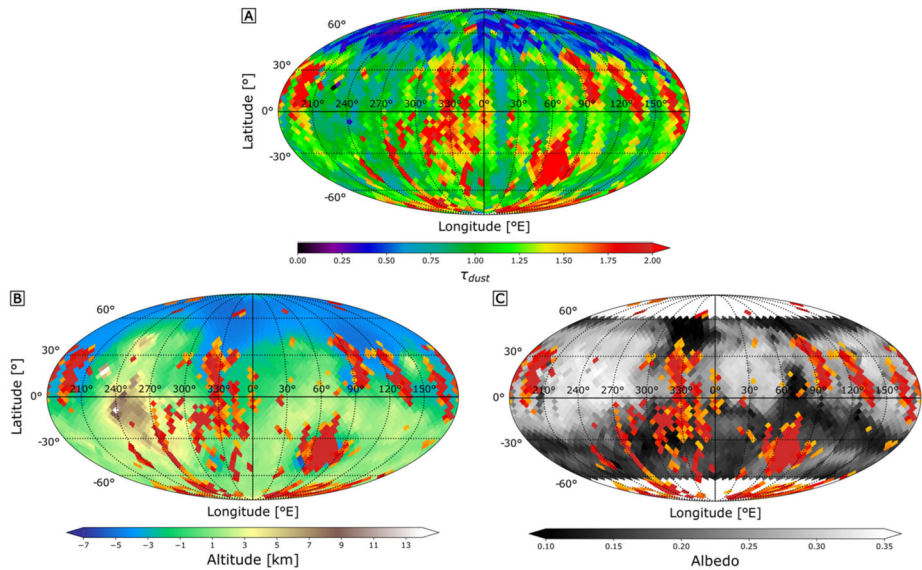


**Fig. 3** [A] Global map of maximum DOD values at a wavelength of  $0.9 \mu\text{m}$  observed by OMEGA between late MY 26 and early MY 30 (excluding the MY 28 GDS), based on Leseigneur and Vincendon (2023). The main dust optical depth features ( $\geq 1.5$ ) are overlaid on a MOLA/MGS topographic map [B] and on a bolometric albedo [C] map made from OMEGA data (Vincendon et al. 2015)

effective radius decreases from  $1.5 \mu\text{m}$  to  $1.1 \mu\text{m}$  during the decay of the MY 28 GDS (Leseigneur and Vincendon 2023; Vincendon et al. 2009), which can be explained by a faster settling of larger particles.

## 2.2 Diurnal Variability

Exploiting the non-Sun-synchronous nature of Mars Express orbit, PFS has performed observations of the Martian atmosphere at all local times (LTs), allowing for the first time the complete characterization of how DODs vary throughout the day on Mars (Wolkenberg and Giuranna 2020; Giuranna et al. 2021).

DOD behaves differently during GDSs (Fig. 4) than in the first half of Martian year (Fig. 5). Figure 4 shows characteristic differences in DOD between morning/noon and evening for MY 28 and MY 34. For both global dust storms, the spatially and seasonally averaged DODs are larger (up to 3) for LTs between 10 and 12 in the core of the storms and drop to minimum values (0.5 or lower) late in the evening (20–22LT). Intermediate values of DODs (0.5–1.5) are observed at 8–9 LT. Especially in MY 28, the contrast between DODs in the morning and evening is still large even during the decay phase. As the data are sparse, the Figures represent the average behavior of the daily cycle over a period of few sols.

Similarly to GDSs, the less intense DOD contrast is observed in all types of storms (A, B, C) defined by Kass et al. (2016) over sub- and tropics during a typical dusty season (Fig. 10 in Wolkenberg and Giuranna 2020). Only in A type storms, DOD is elevated over the SH during all LTs. The similar elevated DOD with its maximum between LT 15 and 17 are observed over the South Pole in type B storms. This maximum repeats from midday in type C storms. For the other LTs, the atmosphere over southern polar regions ( $>70^\circ\text{S}$ ) is relatively dust free. However, these observations have large standard deviations.



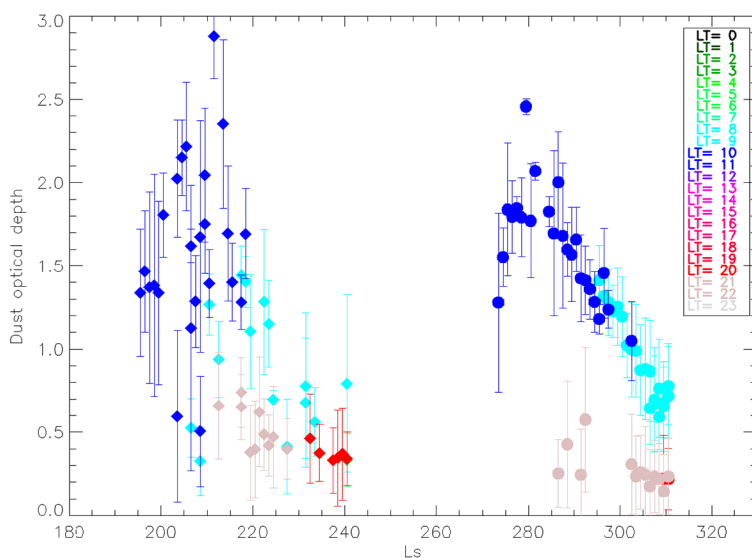


**Fig. 4** DOD at 9.3  $\mu\text{m}$  observed by PFS as a function of Ls ( $1^\circ$  bins) and LT (colours shown in the legend) in the core of MY 28 (Ls = 273–310, circles) and MY 34 (Ls = 195–240, diamonds) GDSs for the southern hemisphere ( $0\text{--}40.5^\circ\text{S}$ ). The error bars show the standard deviation of the averaged values and provide an indication of the observed zonal and meridional variations that are particularly large during a GDS. Based on (Wolkenberg and Giuranna 2020; Giuranna et al. 2021)

The first half of the Martian year presents low dust activity (Fig. 2). Figure 5 shows mean DODs in both hemispheres with similar local time behavior. The main observed feature is a minimum of DOD (0.03–0.04) registered 3 AM and 5 AM. The minimum of the dust content observed in the night/early morning is related to the formation of water ice clouds predicted by a model at these LTs (Hinson and Wilson 2004). In contrast, dayside mean DOD (7 AM–5 PM) shows near constant values ranging between 0.12 and 0.15, in agreement with previous observations at 2–3 PM during non-dusty seasons. A threefold increase in dust was also observed by the MCS-MRO radiometer between night and day during the northern solstice (Heavens et al. 2011a, 2011b, 2011c).

### 2.3 Dust Storms and Devils of Different Sizes

Dust devils on Mars occur in preferred regions such as Arcadia Planitia, Syrtis Major, Thaumasia Planum, Syria Planum, and Amazonis Planitia. These regions are predisposed to the occurrence of these phenomena because of their high surface dust coverage and probably also due to a high regional albedo contrast causing high thermal contrasts, which in turn trigger dust devils at their boundaries (Reiss et al. 2011; Cantor et al. 2006). Thanks to the ability of the HRSC to observe the Martian surface with its nine different channels nearly simultaneously, not only the height, the diameter, and the direction of dust devils, but also their velocity can be estimated by analyzing the positional shift of the features between the images of the different HRSC channels. Stanzel et al. (2006, 2008) analyzed dust devils in different regions on Mars and determined velocities in the range of 1–59 m/s, depending on the size of the dust devil, with a mean value on the order of 20 m/s. Smaller dust devils ( $\sim 1$  km high) travel at about 1.5 to 6 m/s (Stanzel et al. 2006).

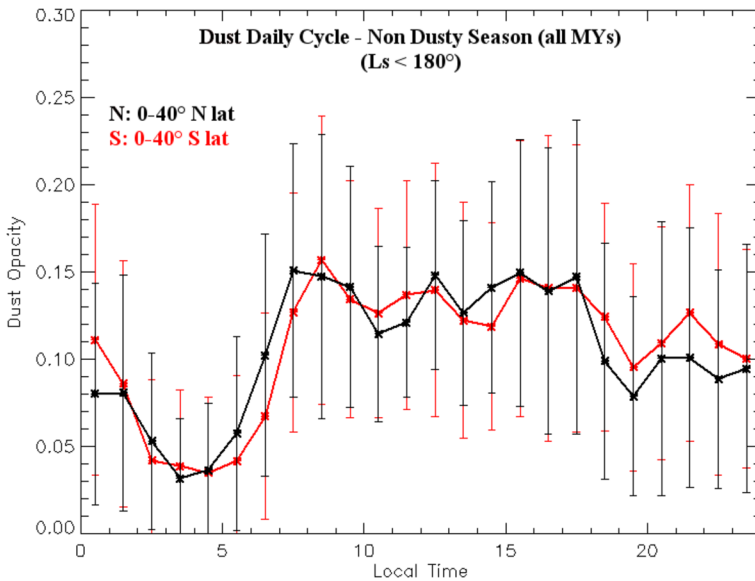


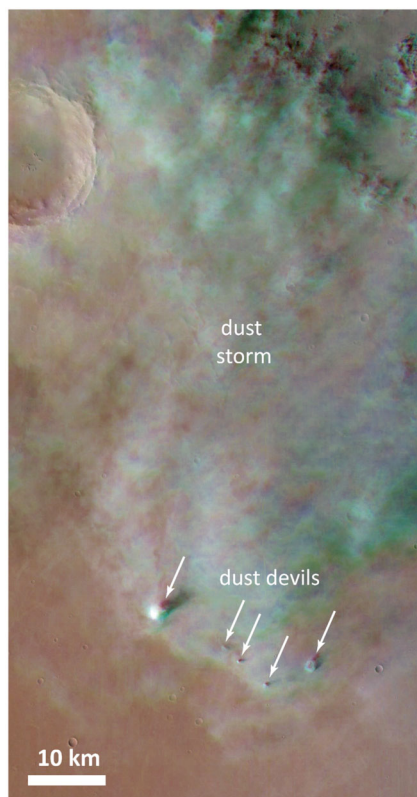
**Fig. 5** DOD at 9.3  $\mu\text{m}$  observed by PFS as a function of Local Time during non-dusty seasons, for the indicated seasonal and latitudinal ranges. The error bars represent the standard deviation of the averages and provide an indication of the zonal, meridional, and inter-annual variations. Reproduced with permission from Giuranna et al. (2021), copyright by Elsevier

The HRSC has captured the tracks left by the largest dust devils and in some cases the dust plumes they raise (Reiss et al. 2011). These dust devils were observed in Syria Planum at latitude  $14.1^{\circ}\text{S}$  and longitude  $251.3^{\circ}\text{E}$  (Fig. 6). Combined with near-simultaneous images obtained with the MOC - Wide Angle (MOC-WA), it was possible to measure translational velocities in the range 3 to 22 m/s for dust devils with sizes of about 700 m and typical lifetimes of 20–30 minutes. One conclusion of Reiss et al. (2011) was that large dust devils (>300–1000 m in size) are active for much longer periods of time than smaller ones, as is the case on Earth. These large dust devils may contribute, at least regionally, to about 50% of dust entrainment into the atmosphere as compared to the smaller dust devils according to a size-frequency distribution power-law.

Using the Visual Monitoring Camera (VMC) and HRSC it has been possible to study the evolution and properties of different types of local and regional dust storms, in particular those occurring at the edge of the northern polar cap during springtime ( $L_s = 0\text{--}90^{\circ}$ ). These disturbances exhibited a rich morphology with textured patterns, spirals, filamentary (arc-shaped) and compact irregular forms that evolve rapidly on a daily basis. They reach 1000–2000 km in extent and are triggered by the intense temperature gradient between the receding polar cap ices and the surrounding terrain, enhanced by the topography (Sánchez-Lavega et al., 2022). VMC captured one of these large, arc-shaped storms (650 km) at the Martian limb showing that the aerosols reached top altitudes of 65 km (Sánchez-Lavega et al. 2018a). Some areas of their textured interiors exhibit organized patterns of clusters of cells formed by 100 elements typically  $\sim 5\text{--}30$  km in size with top altitudes of  $\sim 6\text{--}11$  km above their surroundings as determined from the shadows they cast. The cellular patterns suggest they form by shallow dry convection when the dust is heated and air parcels become buoyant, producing the updrafts (Sánchez-Lavega et al., 2022). The study of a local dust storm in the Atlantis Chaos region in March 2005 with the OMEGA imaging spectrom-



**Fig. 6** Pansharped RGB composite of HRSC orbit h2025\_0000 showing a regional dust storm and dust devils (white arrows) analyzed in Thaumasia Planum by Stanzel et al. (2008) (see also Gwinner et al. 2016). The slight colour offset at the margins of the dust storm and the dust devils is most presumably an indication for the movement of these features between the acquisition of the individual red, green and blue channels



ter revealed that at the center of the storm the size of the dust particles was  $1.6 \mu\text{m}$  where the optical depth at a wavelength of  $9.3 \mu\text{m}$  (silicate absorption band) was  $>7$  (Oliva et al. 2018). Dust reached top altitudes above 18 km and at the surface the dust was deposited in a layer with a thickness of about  $1 \mu\text{m}$  at the storm boundary but  $100 \mu\text{m}$  at its center. The local topography and local thermal inertia probably played a role in the origin and properties of this storm.

After 11 years without a global dust storm, the onset of a new one took place at the end of May 2018 (MY 34) in the Acidalia Planitia region in the NH ( $31^\circ\text{N}$ ,  $12^\circ\text{W}$ ), the location of the storm being something never observed before (Sánchez-Lavega et al. 2019). Also, the storm onset was one of the earliest, occurring at  $L_s = 184^\circ$ . The storm expanded rapidly, primarily to the East and South, with peak velocities of 40 m/s (Sánchez-Lavega et al. 2019). The MEX polar orbit allowed VMC to follow in detail the penetration of the storm into the North polar region (Hernández-Bernal et al. 2019). The polar circulation organized the dust in curved arcs of 2000–3000 km in length that reached heights of up to 70 km while moving rapidly with speeds of 100 m/s (Hernández-Bernal et al. 2019).

Wolkenberg et al. (2020) made a comparative study of the GDSs that occurred in MY 25 (GDS 2001), MY 28 (GDS 2007) and MY 34 (GDS 2018) using data from observations performed by PFS-MEX and TES-MGS and found that the storms in MY 25 and MY 28 dissipated over a very long timescale compared to the storm of MY 34.

## 2.4 Dust Optical Properties

The optical properties of dust are described by the three wavelength-dependent single scattering parameters: phase function (PF), single scattering albedo (SSA), and extinction cross section. Before MEX, the work of Ockert-Bell et al. (1997) based on the Imaging Spectrometer (ISM/Phobos-2) data and Tomasko et al. (1999) on Mars Pathfinder data provided the optical properties of dust in the near-IR.

The spectral variations of the SSA are primarily related to the composition of the grain. The absolute value of the parameter depends also on the average size of the particles (smaller grains have a higher albedo). The analysis of OMEGA data allowed to better constrain SSA, using a local, optically thick dust storm detected at the beginning of the mission (Vincendon et al. 2007; Määttänen et al. 2009). OMEGA data revealed that the Martian dust is brighter in the near infrared than previously thought: the SSA was found to be about 0.97–0.975 between 1  $\mu\text{m}$  and 2.5  $\mu\text{m}$  (Vincendon et al. 2007; Määttänen et al. 2009), while it was previously evaluated to be equal to 0.94 over most of this range (Ockert-Bell et al. 1997). Analysis of CRISM data subsequently confirmed this trend, with a value of 0.965 (Wolff et al. 2009). This high SSA corresponds to optically thick dust in the thickest parts of dust storms, as well as surface covered by dust (Vincendon et al. 2007; Määttänen et al. 2009; Oliva et al. 2018). At longer wavelengths, atmospheric dust contains a broad absorption band at 3  $\mu\text{m}$ , similarly to the surface (Määttänen et al. 2009). This band could reflect the presence of an  $\text{H}_2\text{O}/\text{OH}$ -rich phase in the mineralogical composition of the dust, and/or the presence of adsorbed water at the surface of the grains (see the discussion in Fedorova et al. 2002; Beck et al. 2015 and Stcherbinine et al. 2021).

The relative wavelength variations of the optical depth have also been constrained (Vincendon et al. 2007, 2008, 2009). These wavelength variations depend on the effective cross section (and the particle size). The optical depth ratio  $\tau(1 \mu\text{m})/\tau(2.5 \mu\text{m})$  shows spatio-temporal variations in the OMEGA dataset (Vincendon et al. 2007, 2008), which are interpreted as resulting from variations in particle size (Vincendon et al. 2009). This ratio is usually near 2 and results in a decreasing reflectance slope between  $\lambda = 1 \mu\text{m}$  and  $\lambda = 2.5 \mu\text{m}$  typical of spectra with a significant atmospheric dust contribution (Vincendon et al. 2009). Particle size variations inferred from these ratios are commonly 1.5  $\mu\text{m}$   $\pm$  0.5  $\mu\text{m}$  (Vincendon et al. 2009).

The PF of the dust has also been constrained using multi-angular OMEGA measurements obtained by varying either the solar zenith angle (Vincendon 2013) or the emission angle (Vincendon et al. 2008). The Henyey–Greenstein PF with an asymmetry parameter of 0.63 used by Ockert-Bell et al. (1997), or that of Tomasko et al. (1999) derived from Pathfinder data, both provide a satisfactory explanation of these observations (Vincendon 2013), which seems broadly consistent with recent studies based on another dataset (Chen-Chen et al. 2019, 2021). In particular, the OMEGA dataset was used to probe the backscattering phase angle range (5–30° phase angle, or 150–175° scattering angle). The observed 5–10% backscattering peak can be explained by the surface PF (Vincendon 2013), i.e., meaning that a major backscattering peak in the atmospheric dust PF is not necessary. This is in agreement with the Wolff et al. (2010) analysis of the UV MARCI dataset.

A complete set of parameters for the 0.5–2.5  $\mu\text{m}$  solar range (PF, SSA, and extinction cross section) compatible with OMEGA data and derived from the work of Wolff et al. (2009), is presented in Vincendon et al. (2015). Work is ongoing to further update dust optical parameters according to OMEGA data (Wolff et al. 2019a).

## 3 Water Ice Clouds at Low Altitudes

### 3.1 Global Climatology

The water ice cloud optical depth (COD) can be retrieved with instruments aboard MEX (SPICAM, OMEGA, and PFS). The work of Mateshvili et al. (2007) used SPICAM-UV nadir measurements to derive the COD and obtained a climatology for the first Martian year of SPICAM observations (MY27). They observed the different stages of the aphelion cloud belt (ACB) occurring at low latitudes in agreement with previous work (Smith 2004): the formation of the ACB around  $L_s = 20^\circ$ , being most prominent after aphelion ( $L_s = 71^\circ$ ), and beginning to decay after  $L_s = 140^\circ$  (see Fig. 7 of the seasonal distribution obtained by Willame et al. (2017), discussed below). A set of north polar summer clouds were observed between aphelion and the start of the ACB decay phase ( $L_s = 90\text{--}140^\circ$ ), which were followed by the formation of the north polar hood, in agreement with Wang and Ingersoll (2002). Very few low-altitude ( $<50$  km) clouds were detected after  $L_s = 200^\circ$ , and these were limited to mountain features. A comparison of the cloud cover between MY 27 and 28 was obtained in a following study (Mateshvili et al. (2009)). The seasonal trends were very similar in both years, and the ACB CODs began with a thin haze (values 0.1–0.3) and grew optically thick (0.3–1.0) by the end of Northern spring; however, the end of MY 28 was punctuated by very strong regional dust storms ( $L_s = 270\text{--}310^\circ$ ), which resulted in optically thinner clouds due to the warmer atmospheric temperatures. After four Martian years (MY 27–30) of data acquisition, the SPICAM UV nadir observations were revisited by Willame et al. (2017). They used an improved calibration for SPICAM data (Montmessin et al. 2017) and an updated radiative transfer code with improved aerosol scattering properties (Wolff et al. 2010, 2019b). This extended dataset (Fig. 7) confirmed the climatology of the ACB and polar hood formation in agreement with previous studies (Smith 2004, 2009; Benson et al. 2010, 2011, 2003, 2006). The ACB forms between  $L_s = 20\text{--}30^\circ$  reaching its maximum extent around aphelion ( $L_s = 80\text{--}140^\circ$ ). The ACB is planet-encircling, at or just north of the equator, with the largest average extent over the Tharsis bulge. The edges of the polar hoods were occasionally observed on these four MYs, and their formation began well before the equinoxes. The North Polar Hood formation began towards the end of northern summer, between  $L_s = 160\text{--}200^\circ$ , and the South Polar Hood was visible between  $L_s = 330\text{--}360^\circ$ .

More than six full Martian years (from MY 26,  $L_s = 331^\circ$ , to MY 33,  $L_s = 78^\circ$ ) of data collected by PFS allowed to build the full climatology of water ice with unprecedented coverage and details (Giuranna et al. 2021). Thanks to the large sensitivity and robust radiometric calibration of PFS, this huge dataset allowed the unique retrieval of ice opacity over cold surface areas and in the polar regions, including the polar nights, notoriously difficult to observe. The most prominent feature seen in the PFS climatology is the seasonal extent, pattern and thickness of the North Polar Hoods (NPH), where most of the thickest clouds are observed (Fig. 8). The NPH exhibits large CODs, always extends to the pole and does not completely retreat in northern summer, while the South Polar Hood (SPH) is an optically thinner annular ring that basically follows the climatological latitudes of the seasonal (water) ice cap edge. One of the possible explanations for this is the extremely low atmospheric temperatures of the southern fall and winter, and the corresponding low water content combined with a less efficient supply of water vapour to the southern polar region (Giuranna et al. 2021; Montmessin et al. 2004; Benson et al. 2010; Navarro et al. 2014), but possible interactions with the dust cycle could also be investigated through modelling in the future. The NPH also shows peculiar features, observed in detail by PFS for the first time, with characteristic spatial and seasonal patterns that repeat every Martian year. From  $L_s =$

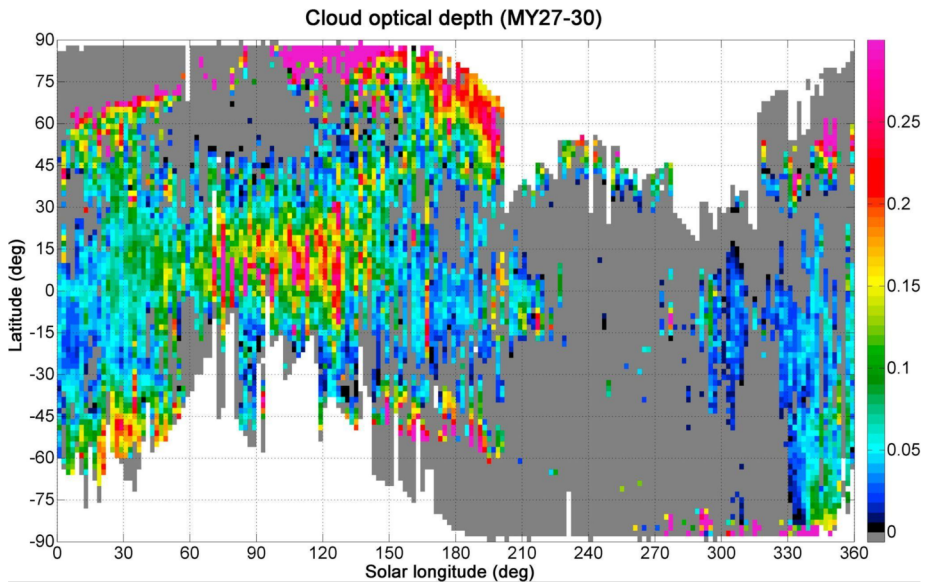


**Fig. 7** Combined seasonal distribution of the zonally averaged water ice COD at 300 nm derived from SPICAM UV nadir observations from MYs 26–30. Reproduced from Willame et al. (2017, licensed under CC BY-NC-ND 4.0)

270° to  $L_s = 360^\circ$ , the whole polar region is covered with optically thick water ice clouds. However, there is a region (50–75°N) where practically no ice clouds form during the entire northern fall. This cloud-free region is observed every Martian year at  $L_s = 170^\circ$ – $280^\circ$ . Its temporal duration is around 60° of solar longitude, but it moves southwards as the season advances (Fig. 8). This feature is not reproduced by current models and, similarly to the dust-free region discussed in Sect. 2.1, a straightforward explanation is still missing. The ACB formation has also been observed by the PFS. The geographic effects of large impact craters on cloud formation are evident, with persistent cloud formations observed over Hellas Planitia, especially its northern edge, and Argyre Planitia. This is in good agreement with OMEGA observations presented in Szantai et al. (2021) and discussed below (Fig. 10). The extent of the ACB, in terms of latitude and  $L_s$ , is in excellent agreement with previous observations, including those from SPICAM (Fig. 7) and OMEGA (Fig. 9).

The VMC has also been used to identify dust and ice hazes at the Martian limb (Sánchez-Lavega et al. 2018a) and combined with other datasets such as MARCI and OMEGA to build a three-dimensional picture of meteorological phenomena. See Sects. 3.3 and 5.3 and Sánchez-Lavega et al. (2024), this collection.

The OMEGA instrument multi-spectral images were used by Madeleine et al. (2012) who demonstrated that even optically thin clouds can be detected from the spectra, and their physical properties can be retrieved. The ratio of two wavelengths (3.4  $\mu\text{m}$  and 3.52  $\mu\text{m}$ ) provides the strength of a strong water ice absorption band and can be used to define the Ice Cloud Index (ICI; Langevin et al. 2007). A full radiative transfer inversion can be performed across a wider wavelength range to retrieve the water ice COD and mean effective radius  $r_{\text{eff}}$ . Olsen et al. (2021) applied this technique to the entire OMEGA dataset from MYs 27–30. The overall mean effective radius was found to be  $\sim 2.2 \mu\text{m}$  with a standard deviation of 0.8 and COD of 0.2–2. Within the ACB, a large range of mean effective radii was observed, and

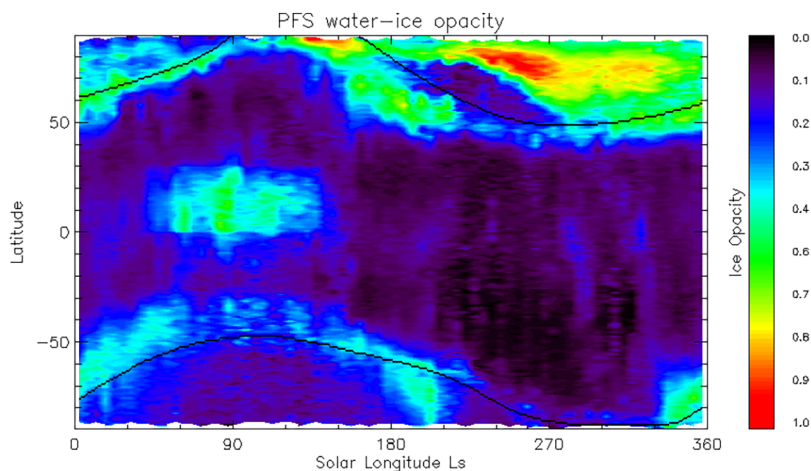


**Fig. 8** Climatology of water ice COD at 12  $\mu\text{m}$  retrieved from nadir PFS observations over MYs 26–33. Reproduced with permission from Giuranna et al. (2021), copyright by Elsevier

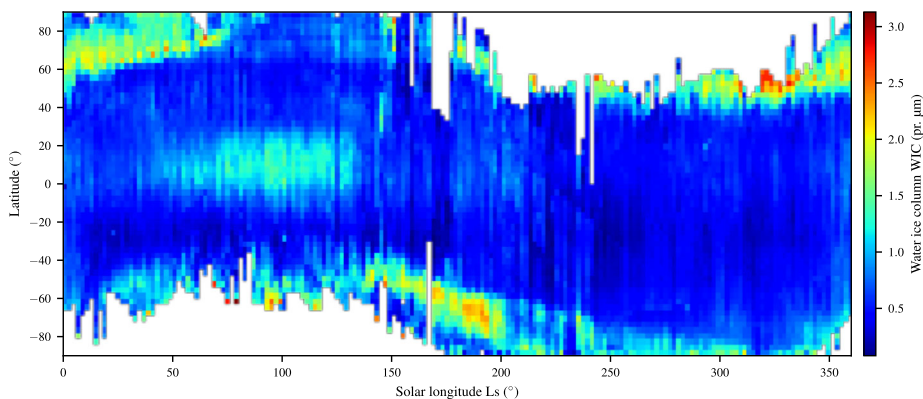


**Fig. 9** OMEGA climatology of the Water Ice Column (WIC; in precipitable  $\mu\text{m}$ , i.e., the thickness of the layer of ice would have if brought down to the surface) estimated from the Ice Cloud Index (ICI), based on the ratio of wavelengths 3.4  $\mu\text{m}$  and 3.52  $\mu\text{m}$ . Data are binned and averaged covering MYs 26–32. Reproduced with permission from Olsen et al. (2021), copyright by Elsevier

different cloud types were identified by Madeleine et al. (2012). The water ice COD and mean effective radius are inversely proportional and can be used to compute the water ice mass in the observed column, and the total Water Ice Column (WIC) in precipitable  $\mu\text{m}$ , defined as the estimated water ice mass divided by the density of water ice. Olsen et al. (2021) demonstrated that the ICI and WIC had a linear dependence, and that a mean climatology of the WIC could be made from the full OMEGA data set recorded spanning MY 26–32, shown in Fig. 9 (Olsen et al. 2021). The North Polar Hood forms around  $L_s = 150^\circ$  and lasts well into the aphelion period. The South Polar Hood is narrower, not forming until the very end of southern summer, around  $L_s = 340\text{--}350^\circ$ , dissipating again in southern spring from  $L_s = 200\text{--}250^\circ$ . The ACB is well defined and most prominent between  $L_s = 40\text{--}140^\circ$  at latitudes between the equator and  $20^\circ\text{N}$ .



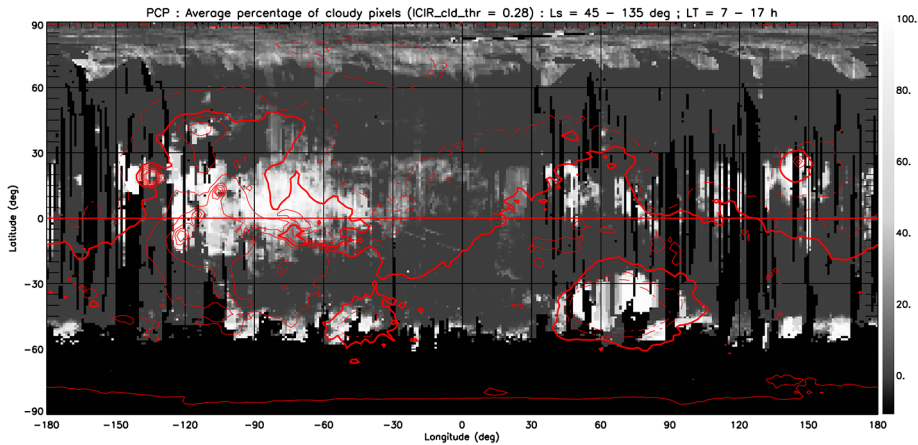


**Fig. 10** Spatial distribution of the PCP in OMEGA multi-spectral images measured over MY 26–32. Observations cover the  $L_s = 45\text{--}135^\circ$ . Adapted from Szantai et al. (2021, licensed under CC BY 4.0)

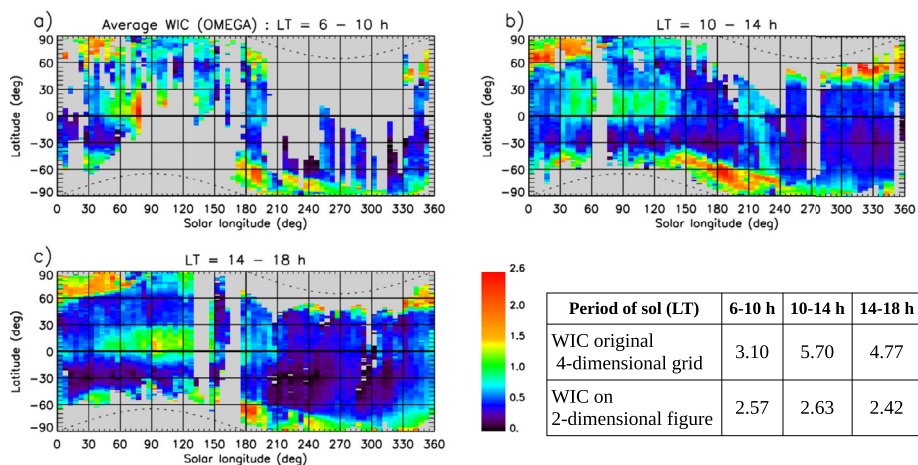
Szantai et al. (2021) studied the distribution and climatology of the reversed ICI that is proportional to cloud thickness ( $ICIR = 1 - ICI$ ) and the percentage of cloudy pixels (PCP) over a grid of  $1^\circ$  latitude and  $1^\circ$  longitude. These parameters, observed over MY 26–32, revealed seasonal variations in the spatial distribution of cloud cover, with higher density ACB clouds forming over the Hellas Planitia and Lunae Planum regions, and where large volcanoes are present. Szantai et al. (2021) defined three climatic zones of interest: a tropical zone ( $25^\circ\text{S}$  to  $25^\circ\text{N}$ ) dominated by the ACB during northern spring and summer; a mid-latitude zone ( $65^\circ\text{S}$  to  $25^\circ\text{S}$  and  $25^\circ\text{N}$  to  $65^\circ\text{N}$ ) affected by the growth and retreat of the polar hoods, and the polar regions, covered for a part of the year by the polar hoods. Other geographic features also impact cloud formation, including large impact basins and large volcanoes.

Figure 10 (Szantai et al. 2021), shows the spatial distribution of the binned percentage of cloudy pixels over the aphelion period between  $L_s = 45\text{--}135^\circ$ . The northern edge of the south polar cap is visible and enhanced ACB cloud coverage is seen over the Tharsis bulge, Hellas Planitia, and over Elysium Mons.

### 3.2 Diurnal Variability

The 4-dimensional (longitude, latitude,  $L_s$ , local time) Ice Cloud Index dataset of OMEGA data covering MY 26 to 32 (Szantai et al. 2021) enables the study of the daily evolution of water ice clouds. Figure 11 shows the diurnal cycle of the WIC over three 4-hour periods (Olsen et al. 2021) as a function of latitude and  $L_s$  averaged over a Martian year. The features that emerge are the polar hoods that are visible during daytime (and when data is available). In the South Polar Hood, more clouds are present around noon (10–14 h LT) than during the afternoon period (14–18 h LT). In the tropics, the ACB shows minimum cloudiness around noon, in agreement with PFS observations (Giuranna et al. 2021). Besides these well-known large-scale cloud features, a lesser-known area and period of cloudiness could be identified. Clouds are also present with a reduced water ice column (or locally limited spatial coverage) in the southern hemisphere, between  $15^\circ\text{S}$  and  $60^\circ\text{S}$ , during northern autumn, between  $L_s = 200^\circ$  and  $240^\circ$ , and during the period around noon (10–14 h LT) (Fig. 11b). These clouds disappear during the afternoon period (14–18 h LT) (Fig. 11c). The





**Fig. 11** Water Ice Column (in  $10^{-3} \text{ kg/m}^2$ , or  $\text{g/m}^2$ ) averaged over all longitudes and over 4-hour periods: 6–10 h LT (a), 10–14 h LT (b), and 14–18 h LT (c). The dashed line shows the polar night terminator. The table gives the maximum values of the original 4-dimensional gridded WIC data, and the maximum values of the averaged WIC on the (2-dimensional) figure. Based on Szantai et al. (2021)

diurnal (and seasonal) life cycle of water ice clouds has also been extracted over specific regions. For example, cloudlike structures were observed in Valles Marineris in the morning around  $L_s = 40^\circ$  by several instruments onboard Mars Express. Based on HRSC images and PFS profiles, Möhlmann et al. (2009) identified these structures as water ice fog. On the other hand, Inada et al. (2008) identified them as dust haze, based on HRSC images and on OMEGA data. The low ICIR values derived from OMEGA data in this area, season, and local time provide evidence that the morning aerosols observed in Valles Marineris were dust particles.

The daily variation of the ACB COD was also characterized with the 6-MY dataset of PFS (Fig. 12). The observed daily cycle of COD shows a nearly symmetric behaviour around noon when the minimum of opacity is observed. The mean COD increases almost linearly from 0.4 at midnight to a peak of 0.6 at 7 AM. The COD then rapidly decreases to a minimum of 0.2 around local noon and increases again to reach a maximum value of 0.6 around 6 PM, similar to that observed in the morning. Then, the ice opacity decreases almost linearly from late afternoon until midnight. Also, the nighttime cloud spatial extent is larger compared to the daytime and a clear minimum is observed around noon. The daily cycle of water ice clouds observed by PFS in the ACB may be interpreted as the result of the i) warm dayside temperatures that prevent part of the water vapour to reach the condensation level; ii) increasing COD from midday to afternoon due to condensation on dust nuclei; and iii) strong nighttime tide-clouds coupling (Giuranna et al. 2021).

### 3.3 Mesoscale Clouds

The double (or annular) cyclone is a well-observed, recurring seasonal phenomenon on Mars (Sánchez-Lavega et al. 2018b). This disturbance of about 700 km in diameter forms during the ACB season, in the NH summer at  $L_s = 120^\circ\text{--}130^\circ$ , near the edge of the northern polar cap (latitude  $60^\circ\text{N}$ ) and longitudes  $70^\circ\text{W}\text{--}110^\circ\text{W}$  (for its dynamics see Sánchez-Lavega

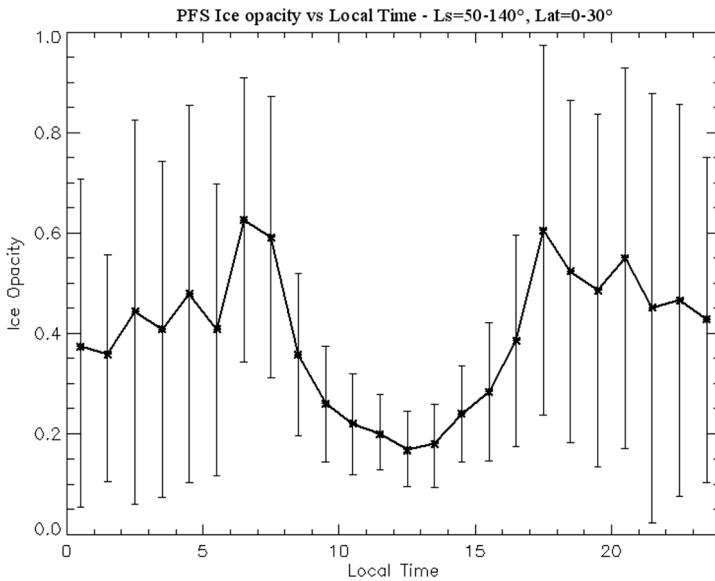


**Fig. 12** Daily variation of mean water ice COD at 12  $\mu\text{m}$  observed by PFS in the aphelion cloud belt, for the indicated seasonal and latitudinal ranges. The error bars represent the standard deviation of the averages and provide indication of the combined zonal, meridional and interannual variations. Reproduced with permission from Giuranna et al. (2021), copyright by Elsevier

et al. 2024, this collection). Images taken from orbit by a variety of cameras including VMC, HRSC and OMEGA from MEX, show that it consists of cirrus, altocumulus and stratus-like water ice cloud patterns (Sánchez-Lavega et al. 2018b) found at an average height of about 10 km. No dust lifting associated with the cyclone is observed. The disturbance grows and appears robust at dawn, but a part of the clouds sublimates and the cyclone loses intensity during the day as insolation increases. The characteristic decaying time of the cyclone suggests water-ice particle sizes of 0.1–1  $\mu\text{m}$  and maximum optical depths of  $\sim 1$ .

Different orographic features on Mars generate mesoscale interactions with the atmosphere. OMEGA has observed lee wave clouds, mostly over the northern plains (Brasil et al. 2022). PFS has contributed to the understanding of thermal circulations around volcanoes (Grassi et al. 2005; Wolkenberg et al. 2010). Orographic clouds are typically observed on Tharsis volcanoes during the aphelion season (e.g., Benson et al. 2006). In contrast, a prominent orographic elongated cloud forming at Arsia Mons during the opposite season ( $L_s = 220^\circ\text{--}320^\circ$ ) has been widely studied based on VMC data, among other instruments. The Arsia Mons Elongated Cloud (AMEC; Hernández-Bernal et al. 2021a) forms over the Western slope of the Arsia Mons volcano every day in the early morning, expands quickly and acquires its characteristic elongated shape, with a length of up to 1800 km, and then dissipates in a few hours. Mesoscale simulations for the perihelion season (Hernández-Bernal et al. 2022) demonstrated that the AMEC and also the other thin clouds observed on Tharsis volcanoes during the perihelion season are the result of vertically propagating gravity waves perturbing the hygropause. This differs from the aphelion season, when orographic clouds on Tharsis are mostly driven by anabatic winds (Michaels et al. 2006)

## 4 Vertical Profiling of Aerosols

### 4.1 Climatology of the Vertical Distribution of Aerosols

Provided they have sufficient altitude resolution, observations made at the limb of Mars (either in a limb staring or in a stellar/solar occultation mode), are a powerful means for studying Martian aerosols. Several aerosol profiles were published before MEX, like the limb images collected by the Viking orbiters (Jaquin et al. 1986) and later from the first solar occultation at Mars performed by the Phobos 2 mission (Korablev et al. 1993). This quote from Jaquin et al. (1986) captures the essence of the Martian haze: “the typical atmospheric column contains one or more discrete, optically thin, ice-like haze layers between 30 and 90 km elevation, depending on season, whose composition is inferred to be water ice. Below the detached hazes there is a continuous haze extending to the surface.” MRO/MCS experiment has also revealed that mineral dust could cause the appearance of more intermittent discrete layers (Heavens et al. 2014).

One of the first studies delivered by MEX on aerosol vertical structure was reported in Montmessin et al. (2006a) using SPICAM/UV stellar occultations on the nightside (Fig. 13). They confirmed what had already been established from Viking and Phobos 2: a seasonally and spatially varying hazetop (altitude where the tangent opacity equals 1) rising from 25 at aphelion to >70 km at perihelion. These data collected in the UV cannot discriminate effective radii  $r_{eff}$  larger than 0.5  $\mu\text{m}$ . The mean aerosol profile observed near the equator matches Jaquin et al.’s (1986) description, with a peak capping a continuous haze that becomes gradually optically thicker towards the surface. Above 60 km, a constant submicron component was found, suggesting the presence of a background population. This submicron component was also reported from limb observations made by SPICAM (Rannou et al. 2006), although the inferred  $r_{eff}$  values (down to 10 nm) are difficult to reconcile with the values derived from stellar occultation. Määttänen et al. (2013) extended these first SPICAM stellar occultation results to more than three Martian years of data and included solar occultations. They established the repetitive behavior of aerosols from year to year: aerosols were found to be lofted systematically higher during the second half of the year. They also found a pronounced equator-to-pole reduction in the haze top altitude that may reveal the average impact of circulation on aerosols over the year.

SPICAM UV data were complemented by data collected in the IR (Fedorova et al. 2009) that also show frequent discrete layers forming above 30 km, sometimes totally detached from the rest of the main haze below. Dust  $r_{eff}$  were generally found in the range 0.5–1  $\mu\text{m}$ , thereby complementing and extending SPICAM UV sensitivity towards larger particle sizes. By combining SPICAM UV and IR observations, a height dependence on particle size could be found (Fedorova et al. 2014). In general, smaller particles (1–2  $\mu\text{m}$ ) are observed at higher altitudes, while larger particles (3–4  $\mu\text{m}$ ) tend to be closer to the surface, in agreement with observations made with other instruments (Clancy et al. 2003; Guzewich et al. 2014).

Other instruments collected images of the Martian limb, revealing the structure of hazes in a broader context. Out of the 21,000 images taken by VMC in 2007–2016, 18 apparitions of high-altitude (40–85 km) aerosols in the limb were analyzed (Sánchez-Lavega et al. 2018a). Three of these events were analyzed in further detail, using additional images from MRO/MARCI and comparing them with the Mars Climate Database (MCD; Millour et al. 2015). Two of these events were cloud features, while the third one was an elevated dust plume from a regional dust storm. VMC also surveyed high-altitude aerosols in the limb during the MY 34 GDS (Hernández-Bernal et al. 2019).

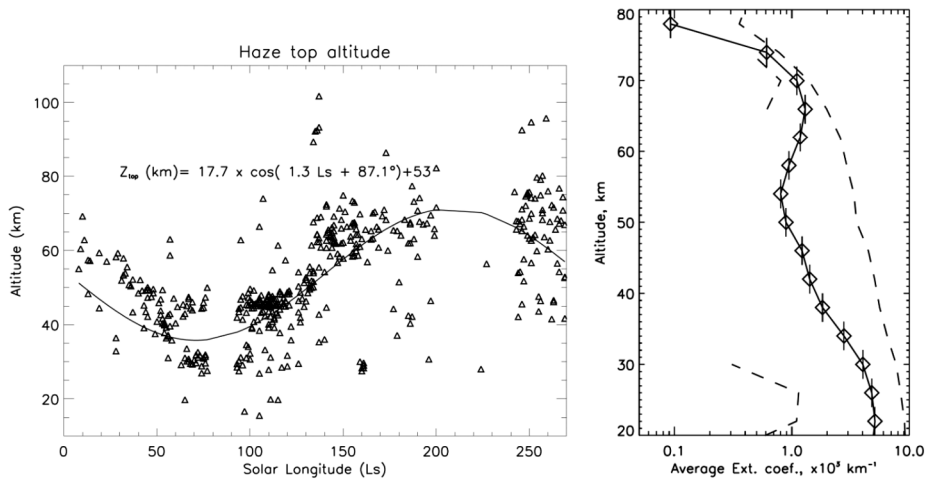


**Fig. 13** (left) the top of the Martian haze corresponding to a unit opacity (in the UV at 250 nm) along the line of sight and showing its evolution with season. (right) the annual mean profile of aerosol extinction observed in the equatorial region. Reproduced with permission from Montmessin et al. (2006a), copyright by Wiley

Despite its hyperspectral capability allowing it to provide compositional information, the OMEGA observations of Mars' limb (Fouchet et al. 2006) have long remained under-exploited. Only recently a study based on these data and focusing on the dust properties was published (D'Aversa et al. 2022). The approach chosen to analyze these data was complex and only allowed to extract information in three cases that were chosen to demonstrate the potential performance of the method. Dust  $r_{eff}$  of the order of  $0.85 \mu\text{m} \pm 0.15$  were derived, in excellent agreement with SPICAM values. Previously, only one OMEGA limb observation containing water ice was used in a study dedicated to mesospheric clouds (Vincendon et al. 2011): it revealed small-grained water particles at very high altitude (see Sect. 5.2). Ongoing work will provide a broader view of dust and water ice in the OMEGA limb dataset (Wolff et al. 2019c).

The limb observations of HRSC are another largely under-exploited dataset that can profile aerosols with sub-km vertical resolution. Although no dedicated study has been published on this data, HRSC atmospheric radiance profiles extracted from limb data were included in a recent exercise that led to constrain the radiometric properties of the Martian limb in preparation of the Mars Sample Return (Slipski et al. 2023). While the scope of the study was essentially technological, it provided, for the first time, HRSC limb profiles together with MRO/MCS profiles showing the typical vertical structure of the Martian aerosols with detached layers overhanging the main dust haze. Interestingly, the profiles were essentially devoid of detached layers with a hazetop located at 40 km for  $L_s = 60^\circ\text{--}100^\circ$ , after which detached layers up to 80 km started to appear frequently. Note that the study basically spanned equatorial latitudes ( $\pm 45^\circ$ ).

With TGO, contrary to the sparse limb and occultation coverage of MEX, aerosol profiles have become a standard and abundant product as the orbiter performs on average 24 solar occultations per day. Several studies on aerosols and clouds have been conducted with TGO data. Fedorova et al. (2020) describe how the GDS affected the vertical distribution of water vapor, ice clouds and dust. A brutal rise of their top altitude from 30 to 70 km marked the onset of the GDS, implying volatile and aerosol upsurge by an intensified global circulation. This first study was followed by a number of others (Stcherbinine et al. 2020, 2022; Liuzzi

et al. 2020, 2021; Luginin et al. 2020) that provided a more detailed view of the behavior of these species, some covering a full Martian year (see Sect. 5.2 and Montmessin et al. 2024, this collection).

## 4.2 Bimodal Particle Size Distribution

Microphysical modeling of cloud formation on Mars required to add a population of sub-micron dust particles in addition to the standard micron mode (Montmessin et al., 2002). Based on Viking limb radiance observations and microphysical modeling, Montmessin et al. (2002) derived a bimodal distribution at  $L_s = 176^\circ / 15^\circ\text{S}$ , featuring an effective radius  $r_{\text{eff}} = 1.8 \mu\text{m}$  and variance  $v_{\text{eff}} = 0.5$  for the large mode and  $r_{\text{eff}} < 0.2 \mu\text{m}$  for the small mode, with population ratio (small to large) of  $\sim 25$ . Markiewicz et al. (1999) reported a possible presence of bimodal distribution based on the IMP (the Imager for Mars Pathfinder) visible sky brightness data at  $L_s \sim 156^\circ$ . On MEX, only the SPICAM UV and IR spectrometers had a possibility to detect the bimodal aerosol distribution. SPICAM UV is sensitive to sub-micron particles ( $0.01\text{--}0.6 \mu\text{m}$ ) above 30 km and the SPICAM IR channel allows probing deeper into the lower atmosphere and is sensitive to particle size up to  $1.5 \mu\text{m}$ . The vertical distribution of aerosols was studied by Fedorova et al. (2014) in 20 solar occultations for the beginning of northern summer in MY29 ( $L_s = 56\text{--}97^\circ$ ). Based on Mie scattering, a bimodal distribution of aerosol was inferred. As SPICAM can't distinguish between dust and ice particles, the coarser mode was modelled assuming  $\text{H}_2\text{O}$  or dust particles: the obtained average radius was equal to  $0.7$  or  $1.2 \mu\text{m}$ , respectively, with number density  $0.01\text{--}10 \text{ cm}^{-3}$ . The finer mode with a radius of  $40\text{--}70 \text{ nm}$  and a number density from  $1 \text{ cm}^{-3}$  at 60 km to  $1000 \text{ cm}^{-3}$  at 20 km was detected. In the SH the finer mode extended up to 70 km, whereas in the NH it was confined below  $30\text{--}40 \text{ km}$ . The submicron mode is unstable against coagulation and its replenishment requires a continuous source of particles (meteoric flux or dust lifted from the surface).

Establishing the detailed characteristics of Martian dust bimodality will require extending this work to the entire joint UV-IR aerosol dataset of SPICAM, and contributions from ACS and NOMAD on TGO. The latter have the advantage that they can distinguish between dust and  $\text{H}_2\text{O}$  ice and even  $\text{CO}_2$  ice (Luginin et al. 2020; Liuzzi et al. 2020, 2021; Stcherbinine et al. 2020, 2022), avoiding the ambiguity in SPICAM measurements.

## 5 Mesospheric Clouds

### 5.1 $\text{CO}_2$ Ice Cloud Climatology

One of the major discoveries of MEX was the first spectroscopic detection of  $\text{CO}_2$  ice clouds outside polar latitudes on Mars and in the mesosphere (Montmessin et al. 2007). There had been earlier indications on the existence of these clouds (Clancy et al. 2007), some provided by MEX through observations of mesospheric  $\text{CO}_2$ -supersaturated cold pockets with adjacent aerosol layers and  $\text{CO}_2$  ice scattering features (Montmessin et al. 2006b; Formisano et al., 2006). Since their detection, several climatologies of  $\text{CO}_2$  ice clouds have been published based on MEX and TGO data (Määttä et al. 2010; Scholten et al. 2010; Aoki et al. 2018; Liuzzi et al. 2021; Oliva et al. 2022) and on MRO data (Vincendon et al. 2011), using both nadir and solar occultation observations. Other mesospheric cloud datasets also surely contain  $\text{CO}_2$  ice clouds, but in lack of compositional information we do not discuss them in this section (see Sects. 5.2 and 5.3).

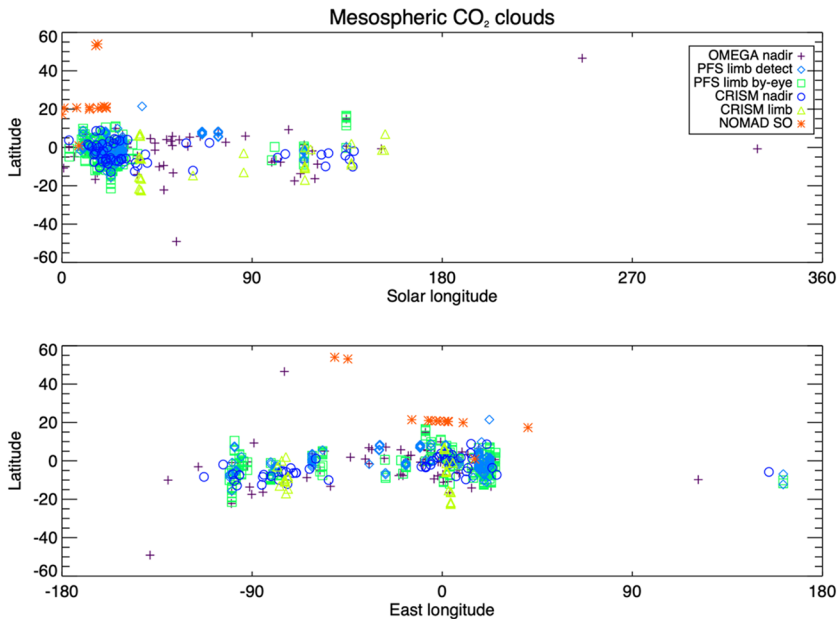


**Fig. 14** Seasonal and geographical distribution of CO<sub>2</sub> ice clouds from MEX, CRISM and TGO. The figure is similar to Fig. 6 in Määttänen and Montmessin (2021), with added NOMAD data. Data sources are: OMEGA nadir: Määttänen et al. (2010) and Vincendon et al. (2011); CRISM nadir: Vincendon et al. (2011); PFS limb: Aoki et al. (2018); CRISM limb: Clancy et al. (2019); NOMAD solar occultations: Liuzzi et al. (2021)

Figure 14 shows the climatology of CO<sub>2</sub> ice clouds from MEX and TGO. The observational coverage is not uniform, but a general picture is emerging from the data. The clouds form around the equator during NH spring and summer ( $L_s = 330^\circ$ – $150^\circ$ ), with a distinct pause around aphelion ( $L_s = 50^\circ$ – $90^\circ$ ). There are also some CO<sub>2</sub> ice detections at midlatitudes during autumn and winter (Montmessin et al. 2007; Määttänen et al. 2010; Liuzzi et al. 2021). The formation of these clouds is thought to happen in mesospheric cold pockets, formed in the interplay between thermal tides and gravity waves (Clancy et al. 2007; Gonzalez-Galindo et al., 2011; Spiga et al. 2012), and the microphysical processes that allow them to form and evolve have been modeled in subsequent work (Listowski et al., 2014; Plane et al., 2018; Määttänen et al. 2022).

The altitudes of the clouds span the mesosphere, from as low as 40 km up to 90 km (Montmessin et al. 2007; Määttänen et al. 2010; Scholten et al. 2010; Liuzzi et al. 2021), and even 100 km during nighttime (Montmessin et al. 2006b). The advantage of solar and stellar occultations is the possibility to probe altitudes and vertical structures of the clouds, and thanks to this opportunity both Montmessin et al. (2006b) and Liuzzi et al. (2021) provided simultaneous temperature retrievals allowing for the estimation of saturation ratios with respect to CO<sub>2</sub> ice. Both studies revealed supersaturated pockets with adjacent aerosol layers that were in the case of Liuzzi et al. (2021) identified as CO<sub>2</sub> ice clouds. The inferred saturation ratios well exceeded ten (Liuzzi et al. 2021).

The great potential of MEX instrument synergies was highlighted in these observations through the use of simultaneous surface-pointing observations of CO<sub>2</sub> ice clouds, where OMEGA provided the composition identification in a narrow swath and HRSC the context with its high-resolution image in addition to an estimation of the cloud altitude (Scholten



et al. 2010). The latter was enabled by the parallax of the high-altitude clouds in off-nadir channel images of HRSC. In addition, the time lag between the images allowed HRSC to provide an estimation of the cross-orbit cloud movement, proportional to mesospheric winds, which are notoriously difficult to measure.

The observations also provided the opportunity to estimate cloud optical depths  $\tau_{\text{CO}_2}$  (at 1  $\mu\text{m}$ ) by using simultaneous views of the cloud and its shadow in OMEGA images (Montmessin et al. 2007; Määttä et al. 2010), showing that  $\tau_{\text{CO}_2}$  remained below 0.5. Later studies found similar optical depth values (Vincendon et al. 2011). Cloud crystal effective radii have been estimated from many datasets, ranging from nanometer range (Montmessin et al. 2006b; Oliva et al. 2022) through micron-size (Montmessin et al. 2007; Määttä et al. 2010; Vincendon et al. 2011) and up to 5  $\mu\text{m}$  (Liuzzi et al. 2021).

## 5.2 Mesospheric Water Ice Clouds

Water ice clouds have also been observed to be present in the Martian mesosphere through occultation and limb observations (e.g., Montmessin et al. 2006a; Vincendon et al. 2011; Clancy et al. 2019, Stcherbinine et al. 2020, 2022; Liuzzi et al. 2020; Luginin et al. 2020). They are associated with lower opacities and smaller particle sizes ( $r_{\text{eff}} \sim 0.1 \mu\text{m}$ : Montmessin et al. 2006a; Stcherbinine et al. 2022) compared to the polar hoods and the ACB observed below 50 km, referred to as type I and II clouds (Clancy et al. 2003). Thus, Montmessin et al. (2006a) introduced an additional category of type III clouds (mesospheric water ice clouds). The coexistence of ice crystals with supersaturated water vapor at very high altitude may play a role in the atmospheric escape and water loss of Mars (Fedorova et al. 2020).

SPICAM UV occultation measurements (Montmessin et al. 2006a) reported the presence above 60 km of thin clouds composed of crystals with  $r_{\text{eff}} \sim 0.1 \mu\text{m}$  associated with opacities at 250 nm between 0.01 and 0.1. Spectroscopic detections of mesospheric water ice clouds were then performed from limb observations acquired by both the OMEGA and CRISM instruments (Vincendon et al. 2011; Clancy et al. 2019), relying on the water ice absorption feature around 3  $\mu\text{m}$ . Vincendon et al. (2011) reported an observation of water ice clouds with  $r_{\text{eff}} = 0.1\text{--}0.5 \mu\text{m}$  at 80 km at  $L_s = 150^\circ$  in midlatitudes. A more extensive monitoring of the properties of mesospheric water ice clouds was then conducted with CRISM (Clancy et al. 2019), where small ice crystals ( $r_{\text{eff}} < 0.2 \mu\text{m}$ ) were typically observed up to 50 km in the aphelion season and up to 70–80 km around the perihelion.

Since 2018, the ACS and NOMAD instruments onboard TGO have significantly contributed to the study of mesospheric water ice clouds thanks to their high sensitivity in IR solar occultations (Fedorova et al. 2020; Stcherbinine et al. 2020, 2022; Luginin et al. 2020; Liuzzi et al. 2020; Streeter et al. 2022). The IR spectral range allows to unambiguously discriminate between dust,  $\text{H}_2\text{O}$  and  $\text{CO}_2$  and the instruments can also detect very thin hazes. The ubiquitous presence of small-grained, thin hazes ( $r_{\text{eff}} \sim 0.1 \mu\text{m}$  and extinction down to a few  $10^{-5} \text{ km}^{-1}$ ) at dawn and dusk has been observed during the whole Martian year, with a maximal altitude of  $\sim 50$  km at aphelion and 80 km at perihelion (Stcherbinine et al. 2022). In addition, TGO instruments have also observed the impact of the MY 34 GDS on the vertical profiles of the aerosols, leading to detections of small-grained mesospheric water ice clouds up to 100 km in the beginning of the storm ( $L_s \sim 200^\circ$ ) (Fedorova et al. 2020; Stcherbinine et al. 2020; Liuzzi et al. 2020; Luginin et al. 2020).

## 5.3 Mesospheric Clouds Seen in Twilight

High-altitude clouds can be seen in twilight illuminated by sunlight when the surface below is in shadow, in analogy with noctilucent clouds on Earth (Hernández-Bernal et al. 2021b).

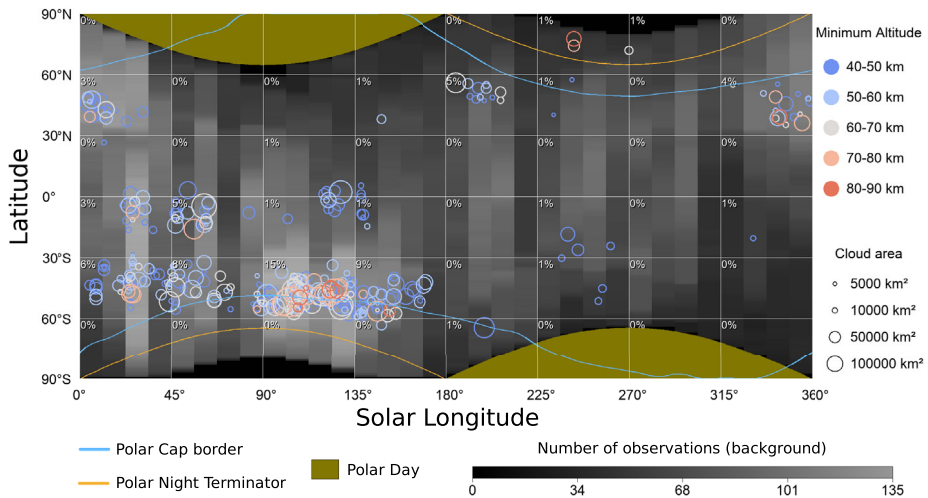


**Fig. 15** Seasonal distribution of mesospheric clouds in twilight as observed by MEX/VMC. For each rectangle of the grid, the percentage of positive observations is indicated in the top-left corner. This figure is analogous to Fig. 4 in Hernández-Bernal et al. (2021b), but the dataset has been updated up to  $L_s = 220^\circ$  in MY 36 and only clouds with minimum altitudes above 40 km are included

From space, clouds in twilight appear near the terminator as bright patches over a dark surface, enabling the detection of thin clouds that would not be visible in nadir. A first-order estimation of the minimum altitude of the cloud can be obtained with simple geometry; however, the parallax of the observation and the non-spherical shape of the planet are not always negligible (Hernández-Bernal et al. 2021b). Contrary to sun-synchronous orbiters, the orbit of MEX is particularly well suited for monitoring morning twilight, visible from the MEX apocenter. The images collected by VMC over 15 years enabled Hernández-Bernal et al. (2021b) to make the first long-term systematic study of these clouds on Mars, finding 409 clouds in twilight. Figure 15 shows the seasonal distribution of the clouds.

The composition of clouds in twilight cannot be determined with VMC, but their climatology can be compared to other mesospheric cloud datasets. Similar trends are present in this climatology as in that of mesospheric  $\text{CO}_2$  clouds (Sect. 5.1); however, clouds in the southern midlatitudes are very common compared to the other locations. The aphelion pause seen for  $\text{CO}_2$  ice clouds is also present both in equatorial and in southern midlatitude clouds. Clouds in northern midlatitudes are absent in  $L_s = 210^\circ\text{--}340^\circ$ , however McConnochie et al. (2010) found many clouds in this latitude and season around the evening twilight; this discrepancy might be due to the lower VMC coverage in the evening.  $\text{CO}_2$  clouds in midlatitudes have been reported by Montmessin et al. (2007), Määttänen et al. (2010) and Liuzzi et al. (2021). In addition to them, Montmessin et al. (2006b) reported four  $\text{CO}_2$  clouds around midnight in latitudes  $15^\circ\text{S}\text{--}40^\circ\text{S}$  and McConnochie et al. (2010) reported mesospheric clouds of unknown composition in northern midlatitudes. Almost all of these midlatitude mesospheric clouds were observed around twilight, except the midnight clouds reported by Montmessin et al. (2006b), and an afternoon cloud in northern midlatitudes reported by Määttänen et al. (2010).

All of these observations suggest that midlatitude mesospheric clouds are mostly present in the morning and the evening. Future observations of clouds in twilight by VMC, HRSC, OMEGA, and other instruments onboard other missions (e.g., the IUVS imager on MAVEN,

as already shown by Connour et al. 2020), will provide a wider coverage, high-resolution observations, and in some cases the composition of these clouds.

## 6 Conclusion and Perspectives

Mars Express has provided a significant amount of observations on Martian clouds and dust, increasing our understanding of atmospheric phenomena on Mars. Different types of weather phenomena at many scales, their occurrence rates and lifetimes, and seasonal and diurnal variations have been investigated. MEX has also provided many pioneering observations and detections, including wind estimates from measurements of traveling speeds of clouds and dust devils. Moreover, the revival of the VMC camera provided more atmospheric observations than foreseen with the initial science payload. Great synergies are at place with both MEX and TGO simultaneously orbiting Mars.

One example of the remaining mysteries about aerosol particles on Mars are high-altitude plumes or clouds observed with telescopes from Earth but not with orbiting instruments (Sánchez-Lavega et al. 2015; Lilensten et al. 2022). MEX instruments PFS, OMEGA and HRSC have collected data that could be used to shed light on this peculiar phenomenon that might reveal new aspects of the Martian atmospheric dynamics and microphysics.

The more we expand our knowledge about the occurrence of atmospheric phenomena, the better we become at detecting, observing and further analyzing them.

**Acknowledgements** The authors thank the International Space Science Institute (ISSI) in Bern, Switzerland for the support. Parts of the studies presented in this paper received funding from the European Union's Horizon 2020 Programme (H2020-COMPET-08-2014) under grant agreement UPWARDS-633127. ASL was supported by Grupos Gobierno Vasco IT1742-22 and by Grant PID2019-109467GB-I00 funded by MCIN/AEI/10.13039/501100011033/. JHB was supported by ESA Contract No. 4000118461/16/ES/ JD, Scientific Support for Mars Express. KSO was supported by the UK Space Agency (ST/T002069/1 and ST/Y000196/1). The PFS experiment was built at the Institute for Space Astrophysics and Planetology (IAPS) of the National Institute for Astrophysics (INAF), and is currently funded by the Italian Space Agency (ASI; agreement number 2018-2-HH.0). The French authors thank support from the French Space Agency CNES. The authors thank the Belgian Science Policy Office (BELSPO) with the financial and contractual coordination by the European Space Agency (ESA) Programme de Développement d'EXpériences scientifiques (PRODEX) office (PEA 4000103401, 4000121493), and from the European Union's Horizon 2020 research and innovation programme under grant agreement No 101004052 (RoadMap project).

**Funding** Open access funding provided by Istituto Nazionale di Astrofisica within the CRUI-CARE Agreement.

## Declarations

**Competing Interests** The authors have no competing interests to declare that are relevant to the content of this article.

**Open Access** This article is licensed under a Creative Commons Attribution 4.0 International License, which permits use, sharing, adaptation, distribution and reproduction in any medium or format, as long as you give appropriate credit to the original author(s) and the source, provide a link to the Creative Commons licence, and indicate if changes were made. The images or other third party material in this article are included in the article's Creative Commons licence, unless indicated otherwise in a credit line to the material. If material is not included in the article's Creative Commons licence and your intended use is not permitted by statutory regulation or exceeds the permitted use, you will need to obtain permission directly from the copyright holder. To view a copy of this licence, visit <http://creativecommons.org/licenses/by/4.0/>.

## References

- Aoki S, et al (2018) Mesospheric CO<sub>2</sub> ice clouds on Mars observed by planetary Fourier spectrometer on-board Mars Express. *Icarus* 302:175–190. <https://doi.org/10.1016/j.icarus.2017.10.047>
- Beck P, Pommerol A, Zanda B, Remusat L, Lorand JP, Göpel C, Hewins R, Pont S, Lewin E, Quirico E, Schmitt B, Montes-Hernandez G, Garenne A, Bonal L, Proux O, Hazemann JL, Chevrier VF (2015) A Noachian source region for the “black beauty” meteorite, and a source lithology for Mars surface hydrated dust? *Earth Planet Sci Lett* 427:104–111. <https://doi.org/10.1016/j.epsl.2015.06.033>
- Benson JL, Bonev BP, James PB, et al (2003) The seasonal behavior of water ice clouds in the Tharsis and Valles Marineris regions of Mars: Mars Orbiter Camera observations. *Icarus* 165:34–52. [https://doi.org/10.1016/S0019-1035\(03\)00175-1](https://doi.org/10.1016/S0019-1035(03)00175-1)
- Benson JL, James PB, Cantor BA, Remigio R (2006) Interannual variability of water ice clouds over major Martian volcanoes observed by MOC. *Icarus* 184:365–371. <https://doi.org/10.1016/j.icarus.2006.03.014>
- Benson JL, Kass DM, Kleinböhl A, et al (2010) Mars’ south polar hood as observed by the Mars Climate Sounder. *J Geophys Res* 115:E12015. <https://doi.org/10.1029/2009JE003554>
- Benson JL, Kass DM, Kleinböhl A (2011) Mars’ North polar hood as observed by the Mars Climate Sounder. *J Geophys Res* 116:E03008. <https://doi.org/10.1029/2010JE003693>
- Bibring JP, et al (2007) Special section: OMEGA/Mars Express Mars surface and atmospheric properties. *J Geophys Res* 112:E08S01. <https://doi.org/10.1029/2007JE002935>
- Brasil F, Machado P, Gilli G, Cardesín-Moinelo A, Silva JE, Espadinha D, Rianço-Silva R (2022) Probing atmospheric gravity waves on Mars’ atmosphere using Mars Express omega data. In: Seventh international workshop on the Mars atmosphere: modelling and observations. (p. 1537)
- Cantor BA, James PB, Caplinger M, Wolff MJ (2001) Martian dust storms: 1999 Mars orbiter camera observations. *J Geophys Res* 106(E10):23653–23687
- Cantor BA, Malin M, Edgett KS (2002) Multiyear Mars Orbiter Camera (MOC) observations of repeated Martian weather phenomena during the northern summer season. *J Geophys Res* 107(E3):5014. <https://doi.org/10.1029/2001JE001588>
- Cantor BA, Kanak KM, Edgett KS (2006) Mars Orbiter Camera observations of Martian dust devils and their tracks (September 1997 to January 2006) and evaluation of theoretical vortex models. *J Geophys Res, Planets* 111:E12002. <https://doi.org/10.1029/2006JE002700>
- Chen-Chen H, Pérez-Hoyos S, Sánchez-Lavega A (2019) Characterisation of Martian dust aerosol phase function from sky radiance measurements by MSL engineering cameras. *Icarus* 330:16–29. <https://doi.org/10.1016/j.icarus.2019.04.004>
- Chen-Chen H, Pérez-Hoyos S, Sánchez-Lavega A (2021) Dust particle size, shape and optical depth during the 2018/MY34 Martian global dust storm retrieved by MSL Curiosity rover navigation cameras. *Icarus* 354:114021. <https://doi.org/10.1016/j.icarus.2020.114021>
- Clancy RT, Wolff MJ, Christensen PR (2003) Mars aerosol studies with the MGS TES emission phase function observations: optical depths, particle sizes, and ice cloud types versus latitude and solar longitude. *J Geophys Res* 108:5098. <https://doi.org/10.1029/2003JE002058>
- Clancy RT, Wolff MJ, Whitney BA, Cantor BA, Smith MD (2007) Mars equatorial mesospheric clouds: global occurrence and physical properties from Mars Global Surveyor thermal emission spectrometer and Mars Orbiter Camera limb observations. *J Geophys Res* 112:E04004. <https://doi.org/10.1029/2006JE002805>
- Clancy RT, Wolff MJ, Smith MD, Kleinböhl A, Cantor BA, Murchie SL, et al (2019) The distribution, composition, and particle properties of Mars mesospheric aerosols: an analysis of CRISM visible/near-IR limb spectra with context from near-coincident MCS and MARCI observations. *Icarus* 328:246–273. <https://doi.org/10.1016/j.icarus.2019.03.025>
- Connour K, Schneider NM, Milby Z, Forget F, Alhosani M, Spiga A, et al (2020) Mars’s twilight cloud band: a new cloud feature seen during the Mars year 34 global dust storm. *Geophys Res Lett* 47:e2019GL084997. <https://doi.org/10.1029/2019GL084997>
- D’Aversa E, Oliva F, Altieri F, Sindoni G, Carrozzo FG, Bellucci G, et al (2022) Vertical distribution of dust in the Martian atmosphere: OMEGA/MEx limb observations. *Icarus* 371:114702. <https://doi.org/10.1016/j.icarus.2021.114702>
- Douté S (2014) Monitoring atmospheric dust spring activity at high southern latitudes on Mars using OMEGA. *Planet Space Sci* 96:1–21. <https://doi.org/10.1016/j.pss.2013.12.017>
- Fedorova AA, Lellouch E, Titov DV, de Graauw T, Feuchtgruber H (2002) Remote sounding of the Martian dust from ISO spectroscopy in the 2.7 μm CO<sub>2</sub> bands. *Planet Space Sci* 50(1):3–9
- Fedorova AA, et al (2009) Solar infrared occultation observations by SPICAM experiment on Mars-Express: simultaneous measurements of the vertical distributions of H<sub>2</sub>O, CO<sub>2</sub> and aerosol. *Icarus* 200(1):96–117. <https://doi.org/10.1016/j.icarus.2008.11.006>

- Fedorova AA, Montmessin F, Rodin AV, et al (2014) Evidence for a bimodal size distribution for the suspended aerosol particles on Mars. *Icarus* 231:239–260. <https://doi.org/10.1016/j.icarus.2013.12.015>
- Fedorova AA, Montmessin F, Korabely O, et al (2020) Stormy water on Mars: the distribution and saturation of atmospheric water during the dusty season. *Science* 367:297–300. <https://doi.org/10.1126/science.aay9522>
- Forget F, Montabone L (2017) Atmospheric dust on Mars: a review, In: 47th international conference on environmental systems, Charleston, SC (USA), July 2017. ICES-2017-175. <http://hdl.handle.net/2346/72982>
- Formisano V, Maturilli A, Giuranna M, D'Aversa E, López-Valverde MA (2006) Observations of non-LTE emission at 4–5 microns with the planetary Fourier spectrometer aboard the Mars Express mission. *Icarus* 182:51–67
- Fouchet T, Bézard B, Drossart P, et al. (2006) OMEGA limb observations of the Martian dust and atmospheric composition. Second workshop on Mars atmosphere modelling and observations, held February 27 - March 3, 2006 Granada, Spain. LMD, IAA, AOPP, CNES, ESA, 2006, p. 223
- Giuranna M, Wolkenberg P, Grassi D, et al (2021) The current weather and climate of Mars: 12 years of atmospheric monitoring by the planetary Fourier spectrometer on Mars Express. *Icarus* 353:113406. <https://doi.org/10.1016/j.icarus.2019.113406>
- González-Galindo F, Määttänen A, Forget F, Spiga A (2011) The Martian mesosphere as revealed by CO<sub>2</sub> cloud observations and general circulation modeling. *Icarus* 216:10–22. <https://doi.org/10.1016/j.icarus.2011.08.006>
- Grassi D, Fiorenza C, Zasova LV, Ignatiev NI, Maturilli A, Formisano V, Giuranna M (2005) The Martian atmosphere above great volcanoes: early planetary Fourier spectrometer observations. *Planet Space Sci* 53(10):1053–1064
- Guzewich SD, Smith MD, Wolff MJ (2014) The vertical distribution of Martian aerosol particle size. *J Geophys Res* 119:2694–2708. <https://doi.org/10.1002/2014JE004704>
- Gwinner K, Jaumann R, Hauber E, Hoffmann H, Heipke C, Oberst J, Neukum G, Ansan V, Bostelmann J, Dumke A, Elgner S, Erkeling G, Fueten F, Hiesinger H, Hoekzema NM, Kersten E, Loizeau D, Matz K-D, McGuire PC, Mertens V, Michael G, Pasewaldt A, Pinet P, Preusker F, Reiss D, Roatsch T, Schmidt R, Scholten F, Spiegel M, Stesky R, Tirsch D, van Gasselt S, Walter S, Wählisch M, Willner K (2016) The High Resolution Stereo Camera (HRSC) of Mars Express and its approach to science analysis and mapping for Mars and its satellites. *Planet Space Sci* 126:93–138
- Heavens NG, McCleese DJ, Richardson MI, Kass DM, Kleinböhl A, Schofield JT (2011c) Structure and dynamics of the Martian lower and middle atmosphere as observed by the Mars Climate Sounder: 2. Implications of the thermal structure and aerosol distributions for the mean meridional circulation. *J Geophys Res* 116:E01010. <https://doi.org/10.1029/2010JE003713>
- Heavens NG, Richardson MI, Kleinboehl A, Kass DM, McCleese DJ, Abdou W, Benson JL, Schofield JT, Shirley JH, Wolkenberg PM (2011a) Vertical distribution of dust in the Martian atmosphere during northern spring and summer: high-altitude tropical dust maximum at northern summer solstice. *J Geophys Res* 116:E01007. <https://doi.org/10.1029/2010JE003692>
- Heavens NG, Richardson MI, Kleinböhl A, Kass DM, McCleese DJ, Abdou W, Benson JL, Schofield JT, Shirley JH, Wolkenberg PM (2011b) The vertical distribution of dust in the Martian atmosphere during northern spring and summer: observations by the Mars Climate Sounder and analysis of zonal average vertical dust profiles. *J Geophys Res* 116:E04003. <https://doi.org/10.1029/2010JE003691>
- Heavens NG, Johnson MS, Abdou WA, Kass DM, Kleinböhl A, McCleese DJ, et al (2014) Seasonal and diurnal variability of detached dust layers in the tropical Martian atmosphere: detached dust layers in Mars atmosphere. *J Geophys Res, Planets* 119(8):1748–1774. <https://doi.org/10.1002/2014JE004619>
- Hernández-Bernal J, Sánchez-Lavega A, del Río-Gaztelurrutia T, Hueso R, Cardesín-Moinelo A, Ravanis EM, de Burgos-Sierra A, Titov D, Wood S (2019) The 2018 Martian Global Dust Storm over the south polar region studied with MEx/VMC. *Geophys Res Lett* 46:10330–10337. <https://doi.org/10.1029/2019GL084266>
- Hernández-Bernal J, Sánchez-Lavega A, del Río-Gaztelurrutia T, Hueso R, Ravanis E, Cardesín-Moinelo A, et al (2021b) A long-term study of Mars mesospheric clouds seen at twilight based on Mars Express VMC images. *Geophys Res Lett* 48:e2020GL092188. <https://doi.org/10.1029/2020GL092188>
- Hernández-Bernal J, Sánchez-Lavega A, del Río-Gaztelurrutia T, Ravanis E, Cardesín-Moinelo A, Connour K, et al (2021a) An extremely elongated cloud over Arsia Mons volcano on Mars: I. Life cycle. *J Geophys Res, Planets* 126:e2020JE006517. <https://doi.org/10.1029/2020JE006517>
- Hernández-Bernal J, Spiga A, Sánchez-Lavega A, del Río-Gaztelurrutia T, Forget F, Millour E (2022) An extremely elongated cloud over Arsia Mons volcano on Mars: 2. Mesoscale modeling. *J Geophys Res, Planets* 127(10):e2022JE007352
- Hinson D, Wilson RJ (2004) Temperature inversions, thermal tides, and water ice clouds in the Martian tropics. *J Geophys Res* 109:E01002. <https://doi.org/10.1029/JE002129>

- Horne D, Smith MD (2009) Mars Global Surveyor thermal emission spectrometer (TES) observations of variations in atmospheric dust optical depth over cold surfaces. *Icarus* 200:118–128. <https://doi.org/10.1016/j.icarus.2008.11.007>
- Inada A, Garcia-Comas M, Altieri F, Gwinner K, Poulet F, Bellucci G, Keller HU, Markiewicz WJ, Richardson MI, Hoekzema N, Neukum G, Bibring J-P (2008) Dust haze in Valles Marineris observed by HRSC and OMEGA on board Mars Express. *J Geophys Res* 113:E02004. <https://doi.org/10.1029/2007JE002893>
- James PB, Hollingsworth JL, Wolff MJ, Lee SW (1999) North polar dust storms in early spring on Mars. *Icarus* 138:64–73
- James PB, Bonev BP, Wolff MJ (2005) Visible albedo of Mars' south polar cap: 2003 HST observations. *Icarus* 174:596–599
- Jaquin F, Gierasch P, Kahn R (1986) The vertical structure of limb hazes in the Martian atmosphere. *Icarus* 68:442–461. [https://doi.org/10.1016/0019-1035\(86\)90050-3](https://doi.org/10.1016/0019-1035(86)90050-3)
- Kahre MA, Murphy JR, Newman CE, Wilson RJ, Cantor BA, Lemmon MT, Wolff MJ (2017) The Mars dust cycle. In: *The atmosphere and climate of Mars*, vol. 18. p 295
- Kass DM, Kleinboehl A, McCleese DJ, Schofield JT, Smith MD (2016) Interannual similarity in the Martian atmosphere during the dust storm season. *Geophys Res Lett* 43:6111–6118. <https://doi.org/10.1002/2016GL068978>
- Korablev OI, Krasnopolsky VA, Rodin AV, Chassefiere E (1993) Vertical structure of Martian dust measured by solar infrared occultations from the PHOBOS spacecraft. *Icarus* 102:76–87. <https://doi.org/10.1006/icar.1993.1033>
- Korablev O, Montmessin F, Trokhimovskiy A, et al (2018) The Atmospheric Chemistry Suite (ACS) of three spectrometers for the ExoMars 2016 Trace Gas Orbiter. *Space Sci Rev* 214:7. <https://doi.org/10.1007/s11214-017-0437-6>
- Langevin Y, Bibring J-P, Montmessin F, et al (2007) Observations of the south seasonal cap of Mars during recession in 2004–2006 by the OMEGA visible/near-infrared imaging spectrometer on board Mars Express. *J Geophys Res* 112:E08S12. <https://doi.org/10.1029/2006JE002841>
- Leseigneur Y, Vincendon M (2023) OMEGA/Mars Express: a new Martian atmospheric dust hunter. *Icarus* 392:115366. <https://doi.org/10.1016/j.icarus.2022.115366>
- Lilensten J, Dauvergne J-L, Pellier C, Delcroix M, Beaudoin E, Vincendon M, et al (2022) Observation from Earth of an atypical cloud system in the upper Martian atmosphere. *Astron Astrophys* 661:A127. <https://doi.org/10.1051/0004-6361/202141735>
- Listowski C, Määttänen A, Montmessin F, Spiga A, Lefèvre F (2014) Modeling the microphysics of CO<sub>2</sub> ice clouds within wave-induced cold pockets in the Martian mesosphere. *Icarus* 237:239–261. <https://doi.org/10.1016/j.icarus.2014.04.022>
- Liuzzi G, Villanueva GL, Crismani MMJ, Smith MD, Mumma MJ, Daerden F, et al (2020) Strong variability of Martian water ice clouds during dust storms revealed from ExoMars Trace Gas Orbiter/NOMAD. *J Geophys Res, Planets* 125(4):e2019JE006250. <https://doi.org/10.1029/2019JE006250>
- Liuzzi G, Villanueva GL, Trompet L, Crismani MMJ, Piccialli A, Aoki S, et al (2021) First detection and thermal characterization of terminator CO<sub>2</sub> ice clouds with ExoMars/NOMAD. *Geophys Res Lett* 48:e2021GL095895. <https://doi.org/10.1029/2021GL095895>
- Luginin M, Fedorova AA, Ignatiev NI, et al (2020) Properties of water ice and dust particles in the atmosphere of Mars during the 2018 global dust storm as inferred from the atmospheric chemistry suite. *J Geophys Res* 125:e2020JE006419. <https://doi.org/10.1029/2020JE006419>
- Määttänen A, Montmessin F (2021) Clouds in the Martian atmosphere. *Oxford research encyclopedia of planetary science*. Oxford University Press, London. <https://doi.org/10.1093/acrefore/9780190647926.013.114>
- Määttänen A, Fouchet T, Forni O, Forget F, Savijärvi H, Gondet B, Melchiorri R, Langevin Y, Formisano V, Giuranna M, Bibring J-P (2009) A study of the properties of a local dust storm with Mars Express OMEGA and PFS data. *Icarus* 201(2):504–516. <https://doi.org/10.1016/j.icarus.2009.01.024>
- Määttänen A, Montmessin F, Gondet B, Scholten F, Hoffmann H, Hauber E, González-Galindo F, Spiga A, Forget F, Neukum G, Bibring J-P, Bertaux J-L (2010) Mapping the mesospheric CO<sub>2</sub> clouds on Mars: MEx/OMEGA and MEx/HRSC observations and challenges for atmospheric models. *Icarus* 209(2):452–469
- Määttänen A, Listowski C, Montmessin F, Maltagliati L, Joly L, Reberac A, Bertaux J-L (2013) A complete climatology of the aerosol vertical distribution on Mars from MEx/ SPICAM UV solar occultations. *Icarus* 223(2):892–941. <https://doi.org/10.1016/j.icarus.2012.12.001>
- Määttänen A, Mathé C, Audouard J, Listowski C, Millour E, Forget F, González-Galindo F, Falletti L, Bardet D, Teinturier L, Vals M, Spiga A, Montmessin F (2022) Troposphere-to-mesosphere microphysics of carbon dioxide ice clouds in a Mars global climate model. *Icarus* 385:115098. <https://doi.org/10.1016/j.icarus.2022.115098>



- Madeleine J-B, Forget F, Spiga A, et al (2012) Aphelion water-ice cloud mapping and property retrieval using the OMEGA imaging spectrometer onboard Mars Express. *J Geophys Res* 117:E00J07. <https://doi.org/10.1029/2011JE003940>
- Markiewicz WJ, Sablotny RM, Keller HU, Thomas N, Titov D, Smith PH (1999) Optical properties of the Martian aerosols as derived from imager for Mars Pathfinder midday sky brightness data. *J Geophys Res* 104(E4):9009–9017. <https://doi.org/10.1029/1998JE900033>
- Mateshvil N, Fussen D, Vanhellemont F, et al (2007) Martian ice cloud distribution obtained from SPICAM nadir UV measurements. *J Geophys Res* 112:E07004. <https://doi.org/10.1029/2006JE002827>
- Mateshvil N, Fussen D, Vanhellemont F, et al (2009) Water ice clouds in the Martian atmosphere: two Martian years of SPICAM nadir UV measurements. *Planet Space Sci* 57:1022–1031. <https://doi.org/10.1016/j.pss.2008.10.007>
- McCleese DJ, et al (2010) Structure and dynamics of the Martian lower and middle atmosphere as observed by the Mars Climate Sounder: seasonal variations in zonal mean temperature, dust, and water ice aerosols. *J Geophys Res* 115:E12016. <https://doi.org/10.1029/2010JE003677>
- McCleese DJ, Kleinbohl A, Kass DM, Schofield JT, Wilson RJ, Greybush S (2017) Comparisons of observations and simulations of the Mars polar atmosphere. In: VI Mars modeling and observations workshop, Granada, Spain
- McConnochie TH, Bell JF, Savransky D, Wolff MJ, Toigo AD, Wang H, Richardson MI, Christensen PR (2010) THEMIS-VIS observations of clouds in the Martian mesosphere: altitudes, wind speeds, and decameter-scale morphology. *Icarus* 210:545–565. <https://doi.org/10.1016/j.icarus.2010.07.021>
- Michaels TI, Colaprete A, Rafkin SCR (2006) Significant vertical water transport by mountain-induced circulations on Mars. *Geophys Res Lett* 33(16):L16201. <https://doi.org/10.1029/2006GL026562>
- Millour E, et al (2015) The Mars Climate Database (MCD version 5.2), 2015. European Planetary Science Congress 2015 abstr. EPSC2015-438 <http://meetingorganizer.copernicus.org/EPSC2015/EPSC2015-438.pdf>
- Möhlmann D, Niemand M, Formisano V, Savijärvi H, Wolkenberg P (2009) Fog phenomena on Mars. *Planet Space Sci* 57:1987–1992
- Montabone L, Forget F, Millour E, Wilson RJ, Lewis SR, Cantor B, Kass D, Kleinböhl A, Lemmon MT, Smith MD, Wolff MJ (2015) Eight-year climatology of dust optical depth on Mars. *Icarus* 251:65–95
- Montmessin F, Rannou P, Cabane M (2002) New insights into Martian dust distribution and water-ice cloud microphysics. *J Geophys Res* 107(E6). <https://doi.org/10.1029/2001JE001520>
- Montmessin F, Forget F, Rannou P, et al (2004) Origin and role of water ice clouds in the Martian water cycle as inferred from a general circulation model. *J Geophys Res* 109:E10004. <https://doi.org/10.1029/2004JE002284>
- Montmessin F, Bertaux J-L, Quémerais E, Korablev O, Rannou P, Forget F, Perrier S, Fussen D, Lebonnois S, Réberac A, Dimarellis E (2006b) Subvisible CO<sub>2</sub> ice clouds detected in the mesosphere of Mars. *Icarus* 183(2):403–410. <https://doi.org/10.1016/j.icarus.2006.03.015>
- Montmessin F, Quémerais E, Bertaux JL, Korablev O, Rannou P, Lebonnois S (2006a) Stellar occultations at UV wavelengths by the SPICAM instrument: retrieval and analysis of Martian haze profiles. *J Geophys Res* 111:E09S09. <https://doi.org/10.1029/2005JE002662>
- Montmessin F, Gondet B, Bibring J-P, Langevin Y, Drossart P, Forget F, Fouchet T (2007) Hyperspectral imaging of convective CO<sub>2</sub> ice clouds in the equatorial mesosphere of Mars. *J Geophys Res* 112:E11S90. <https://doi.org/10.1029/2007JE002944>
- Montmessin F, Korablev O, Lefèvre F, Bertaux J-L, Fedorova A, Trokhimovskiy A, Lacombe G, Reberac A, Maltagliati L, Willame Y, Guslyakova S, Gérard J-C, Stiepen A, Fussen D, Mateshvil N, Määttänen A, Forget F, Witasse O, Leblanc F, Vandaele AC, Marcq E, Sandel B, Gondet B, Schneider N, Chaffin M, Chapron N (2017) SPICAM on Mars Express: a 10 year in-depth survey of the Martian atmosphere. *Icarus* 297:195–216. ISSN 0019–1035. <https://doi.org/10.1016/j.icarus.2017.06.022>
- Montmessin F, Fedorova A, Alday J, Aoki S, Chaffin M, Chaufray J-Y, Encrenaz T, Fouchet T, Knutsen EW, Korablev O, Liuzzi G, Mayyasi MA, Pankine A, Trokhimovskiy A, Villanueva GL (2024) Mars' Water cycle and escape: a view from Mars Express and beyond. *Space Sci Rev* 220
- Mulholland DP, Spiga A, Listowski C, Read PL (2015) An assessment of the impact of local processes on dust lifting in Martian climate models. *Icarus* 252:212–227
- Navarro T, Madeleine J-B, Forget F, Spiga A, Millour E, Montmessin F, Määttänen A (2014) Global climate modeling of the Martian water cycle with improved microphysics and radiatively active water ice clouds. *J Geophys Res, Planets* 119:1479–1495. <https://doi.org/10.1002/2013JE004550>
- Oeckert-Bell ME, Bell JF, Pollack JB, McKay CP, Forget F (1997) Absorption and scattering properties of the Martian dust in the solar wavelengths. *J Geophys Res* 102(E4):9039–9050. <https://doi.org/10.1029/96JE03991>
- Oliva F, Geminale A, D'Aversa E, Altieri F, Bellucci G, Carrozzo FG, Sindoni G, Grassi D (2018) Properties of a Martian local dust storm in Atlantis Chaos from OMEGA/MEX data. *Icarus* 300:1–11. <https://doi.org/10.1016/j.icarus.2017.07.034>

- Oliva F, D'Aversa E, Bellucci G, Carrozzo FG, Ruiz Lozano L, Altieri F, et al (2022) Martian CO<sub>2</sub> ice observation at high spectral resolution with ExoMars/TGO NOMAD. *J Geophys Res, Planets* 127:e2021JE007083. <https://doi.org/10.1029/2021JE007083>
- Olsen KS, Forget F, Madeleine J-B, et al (2021) Retrieval of the water ice column and physical properties of water-ice clouds in the Martian atmosphere using the OMEGA imaging spectrometer. *Icarus* 353:113229. <https://doi.org/10.1016/j.icarus.2019.03.006>
- Plane JMC, Carrillo-Sanchez JD, Mangan TP, Crismani MMJ, Schneider NM, Määttänen A (2018) Meteoric metal chemistry in the Martian atmosphere. *J Geophys Res Planets*: 695–707. <https://doi.org/10.1002/2017JE005510>
- Rannou P, Perrier S, Bertaux J-L, Montmessin F, Korablev O, Rébérac A (2006) Dust and cloud detection at the Mars limb with UV scattered sunlight with SPICAM. *J Geophys Res, Planets* 111:9. <https://doi.org/10.1029/2006JE002693>
- Reiss D, Zanetti M, Neukum G (2011) Multitemporal observations of identical active dust devils on Mars with the high resolution stereo camera (HRSC) and Mars Orbiter Camera (MOC). *Icarus* 215:358–369
- Sánchez-Lavega A, García-Muñoz A, García-Melendo E, Pérez-Hoyos S, Gómez-Forrellad JM, Pellier JM, et al (2015) An extremely high altitude plume seen at Mars' morning terminator. *Nature* 518:525–528. <https://doi.org/10.1038/nature14162>
- Sánchez-Lavega A, Chen-Chen H, Ordoñez-Etxeberria I, et al (2018a) Limb clouds and dust on Mars from images obtained by the Visual Monitoring Camera (VMC) onboard Mars Express. *Icarus* 299:194–205. <https://doi.org/10.1016/j.icarus.2017.07.026>
- Sánchez-Lavega A, Garro A, del Río-Gaztelurrutia T, Hueso R, Ordoñez-Etxeberria I, Chen Chen H, et al (2018b) A seasonally recurrent annular cyclone in Mars northern latitudes and observations of a companion vortex. *J Geophys Res, Planets* 123:3020–3034. <https://doi.org/10.1029/2018JE005740>
- Sánchez-Lavega A, del Río-Gaztelurrutia T, Hernández-Bernal J, Delcroix M (2019) The onset and growth of the 2018 Martian Global Dust Storm. *Geophys Res Lett* 46:6101–6108. <https://doi.org/10.1029/2019GL083207>
- Sánchez-Lavega A, Erkoceka A, Hernández-Bernal J, del Río-Gaztelurrutia T, García-Morales J, Ordoñez-Etxeberria I, Cardesín-Moinelo A, Titov D, Wood S, Tirsch D, Hauber E, Matz K-D (2022) Cellular patterns and dry convection in textured dust storms at the edge of Mars North polar cap. *Icarus* 387:115183. <https://doi.org/10.1016/j.icarus.2022.115183>
- Sánchez-Lavega A, del Río-Gaztelurrutia T, Spiga A, Hernández-Bernal J, Larsen E, Tirsch D, Cardesín-Moinelo A, Machado P (2024) Dynamical phenomena in the Martian atmosphere through Mars Express imaging. *Space Sci Rev* 220:16. <https://doi.org/10.1007/s11214-024-01047-4>
- Scholten F, Hoffmann H, Määttänen A, Montmessin F, Gondet B, Hauber E (2010) Concatenation of HRSC color and OMEGA data for the determination and 3D-parametrization of high altitude CO<sub>2</sub> clouds in the Martian atmosphere. *Planet Space Sci* 58(10):1207–1214
- Siili T, Haberle RM, Murphy JR, Savijarvi H (1999) Modelling of the combined late winter ice cap edge and slope winds in Mars Hellas and Argyre regions. *Planet Space Sci* 47(8–9):951–970
- Slipski M, et al (2023) The radiometric environment for Mars limb observations by the Mars sample return Earth return orbiter. *Adv Space Res* 72(9):4048–4063. <https://doi.org/10.1016/j.asr.2023.07.019>
- Smith MD (2004) Interannual variability in TES atmospheric observations of Mars during 1999–2003. *Icarus* 167:148–165. <https://doi.org/10.1016/j.icarus.2003.09.010>
- Smith MD (2009) THEMIS observations of Mars aerosol optical depth from 2002–2008. *Icarus* 202:444–452. <https://doi.org/10.1016/j.icarus.2009.03.027>
- Spiga A, Lewis SR (2010) Martian mesoscale and microscale wind variability of relevance for dust lifting. *Mars Int J Mars Sci Explor* 5:146–158
- Spiga A, González-Galindo F, López-Valverde M-A, Forget F (2012) Gravity waves, cold pockets and CO<sub>2</sub> clouds in the Martian mesosphere. *Geophys Res Lett* 39:L02201. <https://doi.org/10.1029/2011GL050343>
- Stanzel C, Pätzold M, Greeley R, Hauber E, Neukum G (2006) Dust devils on Mars observed by the high resolution stereo camera. *Geophys Res Lett* 33:L11202. <https://doi.org/10.1029/2006GL025816>
- Stanzel C, Pätzold M, Williams DA, Whelley PL, Greeley R, Neukum G (The HRSC Co-Investigator Team) (2008) Dust devil speeds, directions of motion and general characteristics observed by the Mars Express high resolution stereo camera. *Icarus* 197:39–51
- Stcherbinine A, Vincendon M, Montmessin F, Wolff MJ, Korablev O, Fedorova A, et al (2020) Martian water ice clouds during the 2018 global dust storm as observed by the ACS mid-infrared channel onboard the Trace Gas Orbiter. *J Geophys Res, Planets* 125:e2019JE006300. <https://doi.org/10.1029/2019JE006300>
- Stcherbinine A, Vincendon M, Montmessin F, Beck P (2021) Identification of a new spectral signature at 3  $\mu$ m over Martian northern high latitudes: implications for surface composition. *Icarus* 369:114627. <https://doi.org/10.1016/j.icarus.2021.114627>

- Stcherbinine A, Montmessin F, Vincendon M, et al (2022) A two Martian years survey of water ice clouds on Mars with ACS onboard TGO. *J Geophys Res* 127:e2022JE007502. <https://doi.org/10.1029/2022JE007502>
- Streeter PM, Sellers G, Wolff MJ, Mason JP, Patel MR, Lewis SR, et al (2022) Vertical aerosol distribution and mesospheric clouds from ExoMars UVIS. *J Geophys Res, Planets* 127:e2021JE007065. <https://doi.org/10.1029/2021JE007065>
- Szantai A, Audouard J, Forget F, et al (2021) Martian cloud climatology and life cycle extracted from Mars Express OMEGA spectral images. *Icarus* 353:114101. <https://doi.org/10.1016/j.icarus.2020.114101>
- Toigo AD, Richardson MI, Wilson RJ, Wang H, Ingersoll AP (2002) A first look at dust lifting and dust storms near the south pole of Mars with a mesoscale model. *J Geophys Res* 107(E7):5050. <https://doi.org/10.1029/2001JE001592>
- Tomasko MG, Doose LR, Lemmon M, Smith PH, Wegryn E (1999) Properties of dust in the Martian atmosphere from the Imager on Mars Pathfinder. *J Geophys Res* 104(E4):8987–9008. <https://doi.org/10.1029/1998JE900016>
- Vandaele AC, Lopez-Moreno JJ, Patel MR, et al (2018) NOMAD, an integrated suite of three spectrometers for the ExoMars trace gas mission: technical description, science objectives and expected performance. *Space Sci Rev* 214:80. <https://doi.org/10.1007/s11214-018-0517-2>
- Vincendon M (2013) Mars surface phase function constrained by orbital observations. *Planet Space Sci* 76:87–95. <https://doi.org/10.1016/j.pss.2012.12.005>
- Vincendon M, Langevin Y, Poulet F, Bibring J-P, Gondet B (2007) Recovery of surface reflectance spectra and evaluation of the optical depth of aerosols in the near-IR using a Monte Carlo approach: application to the OMEGA observations of high-latitude regions of Mars. *J Geophys Res* 112:E08S13. <https://doi.org/10.1029/2006JE002845>
- Vincendon M, Langevin Y, Poulet F, Bibring J-P, Gondet B, Jouglet D (OMEGA Team) (2008) Dust aerosols above the south polar cap of Mars as seen by OMEGA. *Icarus* 196:488–505. <https://doi.org/10.1016/j.icarus.2007.11.034>
- Vincendon M, Langevin Y, Poulet F, Pommerol A, Wolff M, Bibring J-P, Gondet B, Jouglet D (2009) Yearly and seasonal variations of low albedo surfaces on Mars in the OMEGA/MEX dataset: constraints on aerosols properties and dust deposits. *Icarus* 200(2):395–405. <https://doi.org/10.1016/j.icarus.2008.12.012>
- Vincendon M, Pilorget C, Gondet B, Murchie S, Bibring J-P (2011) New near-IR observations of mesospheric CO<sub>2</sub> and H<sub>2</sub>O clouds on Mars. *J Geophys Res* 116:E00J02. <https://doi.org/10.1029/2011JE003827>
- Vincendon M, Audouard J, Altieri F, Ody A (2015) Mars Express measurements of surface albedo changes over 2004–2010. *Icarus* 251:145–163. <https://doi.org/10.1016/j.icarus.2014.10.029>
- Wang H, Ingersoll AP (2002) Martian clouds observed by Mars Global Surveyor Mars Orbiter Camera. *J Geophys Res* 107:8-1–8-16. <https://doi.org/10.1029/2001je001815>
- Wang HR, Richardson MI, Wilson JR, Ingersoll AP, Toigo AD, Zurek RW (2003) *Geophys Res Lett* 30(9):1488. <https://doi.org/10.1029/2002GL016828>
- Willame Y, Vandaele AC, Depiesse C, et al (2017) Retrieving cloud, dust and ozone abundances in the Martian atmosphere using SPICAM/UV nadir spectra. *Planet Space Sci* 142:9–25. <https://doi.org/10.1016/j.pss.2017.04.011>
- Wilson C, Titov D, Holmström M, Barabash S, Lundin R, Roatsch T, Jaumann R, Pätzold M, Orosei R, Carter J, Bibring J-P, Giuranna M, Montmessin F, Bertaux J-L, Sánchez-Lavega A (2024) Mars Express scientific payload and its evolution. *Space Sci Rev* 220
- Wolff MJ, Smith MD, Clancy RT, Arvidson R, Kahre M, Seelos F IV, Murchie S, Savijärvi H (2009) Wavelength dependence of dust aerosol single scattering albedo as observed by the Compact Reconnaissance Imaging Spectrometer. *J Geophys Res* 114:E00D04. <https://doi.org/10.1029/2009JE003350>
- Wolff MJ, Clancy RT, Goguen JD, Malin MC, Cantor BA (2010) Ultraviolet dust aerosol properties as observed by MARCI. *Icarus* 208(1):143–155. <https://doi.org/10.1016/j.icarus.2010.01.010>
- Wolff MJ, Clancy RT, Khare MA, et al (2019b) Mapping water ice clouds on Mars with MRO/MARCI. *Icarus* 332:24–49. <https://doi.org/10.1016/j.icarus.2019.05.041>
- Wolff MJ, Vincendon M, Gondet B, Bibring JP, Flittner D (2019c) The MEX/OMEGA Limb Dataset: Description, Analysis Tools, Initial Results. Ninth International Conference on Mars, held 22–25 July, 2019 in Pasadena, California. LPI Contribution No. 2089, id.6094
- Wolff MJ, Vincendon M, Smith MD, Clancy RT, Langevin Y, Arvidson RE, Bibring JP (2019a) An updated dust aerosol model for Mars. American Geophysical Union, Fall Meeting 2019, abstract #P41B-3407
- Wolkenberg P, Giuranna M (2020) Daily dust variation from the PFS MEX observations. *Icarus*. <https://doi.org/10.1016/j.icarus.2020.113823>
- Wolkenberg P, Formisano V, Rinaldi G, Geminale A (2010) The atmospheric temperatures over Olympus Mons on Mars: an atmospheric hot ring. *Icarus* 207(1):110–123

- Wolkenberg P, Giuranna M, Grassi D, Aronica A, Aoki S, Scaccabarozzi D, Saggin B (2018) Characterization of dust activity on Mars from MY27 to MY32 by PFS-MEX observations. *Icarus* 310:32–47. <https://doi.org/10.1016/j.icarus.2017.10.045>
- Wolkenberg P, Giuranna M, Smith MD, Grassi D, Amoroso M (2020) Similarities and differences of global dust storms in MY 25, 28, and 34. *J Geophys Res, Planets* 125:e2019JE006104. <https://doi.org/10.1029/2019JE006104>

**Publisher's Note** Springer Nature remains neutral with regard to jurisdictional claims in published maps and institutional affiliations.